

## Assimilation of surface velocity data into a primitive equation coastal ocean model

Peter R. Oke,<sup>1</sup> J. S. Allen, Robert N. Miller, Gary D. Egbert, and P. M. Kosro

College of Oceanic and Atmospheric Sciences, Oregon State University, Oregon, USA

Received 26 June 2000; revised 29 November 2001; accepted 11 December 2001; published 10 September 2002.

[1] A data assimilation system (DAS) of the wind-driven, mesoscale shelf circulation off the Oregon coast is developed. The DAS assimilates low-pass filtered surface velocity measurements, obtained from land-based high-frequency coastal radar arrays, into a primitive equation coastal ocean model using a sequential optimal interpolation scheme. Inhomogeneous and anisotropic estimates of the forecast error covariances required for the assimilation are assumed to be proportional to typical cross-correlations between modeled variables. These correlations are estimated from an ensemble of model simulations for 18 different summers. Similarly, the observation error covariances are assumed to be proportional to the actual covariances of the observations. A time-distributed averaging procedure (TDAP) that effectively low-pass filters the model forecast for comparison with the observations and introduces the corrections to the model state gradually over time is used in order to overcome problems of data compatibility and initialization. The correlations between direct subsurface current measurements and subsurface currents obtained from model-only and assimilation experiments for the summer of 1998 are 0.42 and 0.78, respectively, demonstrating the effectiveness of the DAS. Our estimates of the error covariances are shown to be appropriate through a series of objective statistical tests. Analysis of the term balances of the model equations show that the dominant modeled dynamical balances are preserved by the DAS and that uncertainties in the spatial variability of the wind forcing are likely to be one source of model error. By varying the relative magnitudes of the estimated forecast and observation error covariances the DAS is shown to be most effective when approximately 80% of the analysis is made up of the model solution. *INDEX TERMS:* 4263 Oceanography: General: Ocean prediction; 4219 Oceanography: General: Continental shelf processes; 4255 Oceanography: General: Numerical modeling; 3337 Meteorology and Atmospheric Dynamics: Numerical modeling and data assimilation; 4516 Oceanography: Physical: Eastern boundary currents; 4594 Oceanography: Physical: Instruments and techniques; *KEYWORDS:* practical data assimilation, numerical modeling, upwelling, high-frequency radar data

**Citation:** Oke, P. R., J. S. Allen, R. N. Miller, G. D. Egbert, and P. M. Kosro, Assimilation of surface velocity data into a primitive equation coastal ocean model, *J. Geophys. Res.*, 107(C9), 3122, doi:10.1029/2000JC000511, 2002.

### 1. Introduction

[2] The purpose of this study is to develop a method for assimilating surface velocity measurements, obtained from land-based high-frequency (HF) radar arrays, into a primitive equation coastal ocean model. To this end a data assimilation system (DAS), designed to model the subinertial, wind-driven continental shelf circulation off the Oregon coast, is developed. Another aim of this study is to determine how much information about subsurface fields in the coastal ocean can be obtained from measurements of surface

currents. Similar questions have been posed with regard to the assimilation of remotely sensed surface measurements obtained from satellites [e.g., Hurlburt, 1986; Ghil and Malanotte-Rizzoli, 1991; Rienecker and Adamec, 1995; Ezer and Mellor, 1997]. Other studies that have dealt with issues relating to assimilation of radar derived current measurements include those of Lewis *et al.* [1998], Scott *et al.* [2000], and Kurapov *et al.* [2002].

[3] The inputs into a DAS include an observing system that provides observational data, a model, prior estimates of the forecast and observation error covariances, and an algorithm that produces an analysis of the model fields. The outputs from a DAS include an analysis that depends on the observations, the model forecast, and the prior error estimates; an assessment of the analysis; posterior error estimates; statistical tests for the prior error estimates; and an assessment of the observing system. For a thorough

<sup>1</sup>Now at School of Mathematics, University of New South Wales, Sydney, New South Wales, Australia.

review of data assimilation techniques the reader is referred to *Bennett* [1992].

[4] For this study, the observing system is an array of SeaSonde HF radars, manufactured by CODAR Ocean Sensors, deployed along the Oregon coast, and the observations are low-pass filtered surface velocity measurements off Newport (44.6°N). The model for this system is the Princeton Ocean Model (POM) [*Blumberg and Mellor*, 1987] that is utilized in a high-resolution domain with Oregon continental shelf and slope topography. The surface velocity measurements are assimilated into the POM using a sequential optimal interpolation scheme that is based on the Physical-space Statistical Analysis System [*Cohn et al.*, 1998]. The corrections to the model state are implemented using a time-distributed averaging procedure (TDAP) that is similar to the incremental analysis updating approach currently utilized by the Data Assimilation Office at NASA/Goddard Space Flight Center [*Bloom et al.*, 1996]. The TDAP overcomes the problem of data compatibility that arises from assimilating low-pass filtered observations into a model that allows fluctuations at all frequencies and the problem of initialization that is a consequence of the fact that primitive equation models are sensitive to introduced changes in their state variables.

[5] Traditionally, forecast error covariances are assumed to be homogeneous, isotropic, and stationary [e.g., *Ruth-erford*, 1972; *Rienecker and Miller*, 1991; *Bartello and Mitchell*, 1992; *Daley*, 1993; *Chen and Wang*, 1999]. We suggest that such assumptions may be invalid for the coastal ocean environment, so a method by which an inhomogeneous, anisotropic and quasi-nonstationary estimate of the forecast error covariances is formulated. The approach taken here assumes that the forecast error covariances are proportional to a universal correlation function that is empirically derived from an ensemble of typical model simulations. We show that this approach is effective for application to the Oregon continental shelf where wind-driven currents are relatively well-correlated over large spatial scales.

[6] The effectiveness of the DAS is demonstrated through a series of assimilation experiments where the analyzed subsurface velocity fields are compared to direct velocity measurements from a moored acoustic Doppler profiler (ADP) for the summer of 1998. Additionally, the prior error statistics are tested for consistency through a series of objective statistical tests.

[7] When data assimilation is utilized, the correction to the model state acts as a forcing term in each prognostic model equation. The role of the correction term in the DAS is investigated through an analysis of the term balances in the depth-averaged alongshore momentum equation and the temperature equation. We find that the dominant dynamical balances are preserved by the DAS and that uncertainties in the spatial variability of the wind forcing are likely to be a primary source of the model error.

[8] The outline of this paper is as follows. Details of the model configuration are presented in section 2, followed by various model-data comparisons of surface and subsurface velocity data for the summer of 1998 in section 3. A description of the details of the assimilation system, including the formulation of the prior error covariances, is presented in section 4. Results from a series of assimilation experiments for the summer of 1998 are presented in

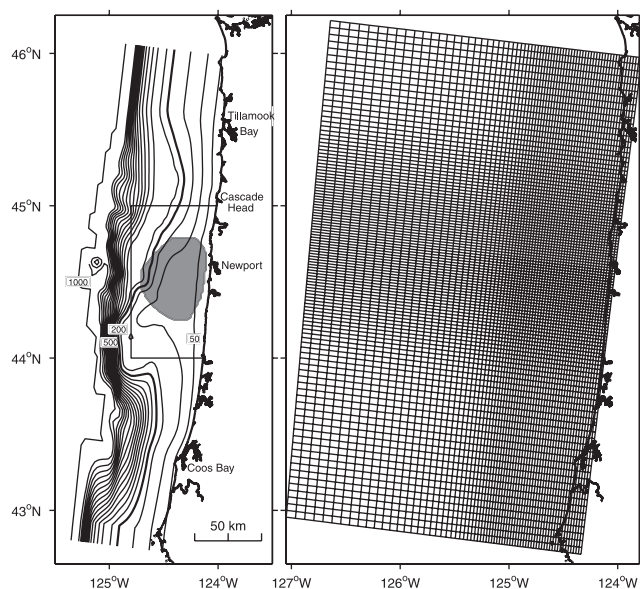


**Figure 1.** (left) Model topography (contour interval = 50 m) showing the CODAR coverage (shading); the 200-m isobath is the thick line. The extent of the detailed topography contoured in Figure 2 is indicated by the box around the CODAR region. (right) Model grid.

section 5. An analysis of the effects of the assimilation on the modeled dynamics is presented in section 6, followed by a summary in section 7. Details of the implementation of the assimilation into the POM are presented in Appendix A, followed by a description of the statistical tests for the prior error estimates in Appendices B and C and an outline of the persistence experiments in Appendix D.

## 2. Model Configuration

[9] For an in-depth discussion of the POM that is utilized here the reader is referred to *Blumberg and Mellor* [1987]. The model grid extends 220 km offshore and 365 km in the alongshore direction (Figure 1). The maximum grid resolution is 2 km over the shelf in the vicinity of Newport (44.6°N), with decreased resolution towards the offshore and alongshore boundaries. The grid is rectangular and the axes have been rotated to 7°N in order to better align with the coastline. The horizontal velocity  $\mathbf{v}$  has components  $(u, v)$  corresponding to the across-shore and alongshore velocities (depth-averages denoted by  $\mathbf{V}$  and  $(U, V)$ ) in the  $(x, y)$  directions, so that  $u$  is positive onshore and  $v$  is positive towards the north (Figure 1). The vertical grid consists of 31 sigma-levels, with eight levels concentrated near the surface, and four near the bottom in order to resolve the respective boundary layers.

[10] The model topography (Figure 1) is linearly interpolated from a 1-km resolution data set and smoothed so that the maximum local slope parameter, defined as the ratio of the depth change to the average depth over each grid cell, is less than 0.18. Experience suggests [*Mellor et al.*, 1994], and unforced experiments [*Barnier et al.*, 1998] with the present model configuration confirm, that if the local slope parameter is less than 0.4 the effect of pressure gradient

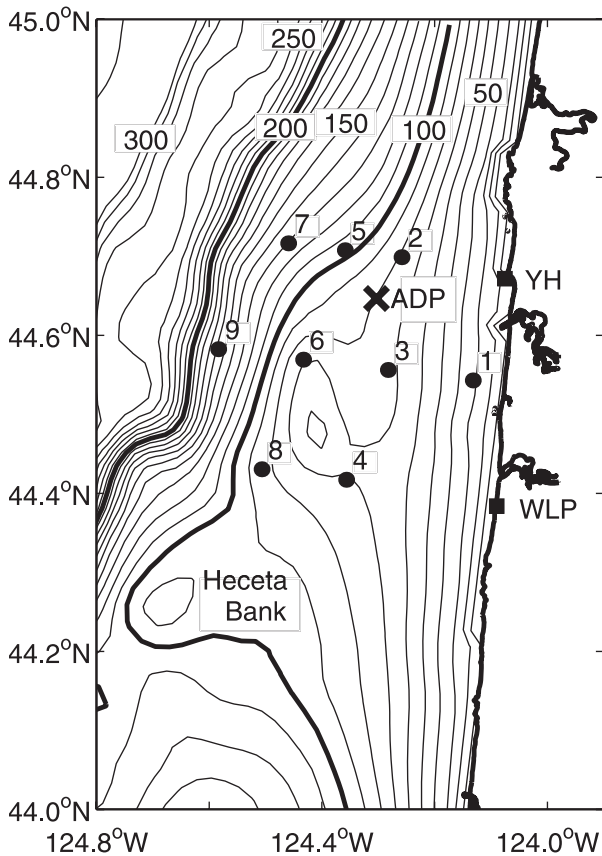


**Figure 2.** Detailed model topography in the CODAR region showing the locations and number of each site at which surface velocity data are assimilated (dots) and the location of the moored ADP (cross). The approximate locations of the radars at Yaquina Head (YH) and Waldport (WLP) are indicated by the squares and the 100- and 200-m isobaths are thick lines.

errors due to the sigma-coordinates is reduced to a tolerable level. A detailed map of the model topography in the CODAR region is shown in Figure 2. The locations of data that are assimilated in the experiments discussed in section 5 are shown, as is the location of the moored ADP that is referred to throughout this manuscript. Only a representative subset of the observations from the CODAR region are used in the assimilation experiments presented in section 5. The minimum depth is 10 m and the maximum depth is set to 1000 m in order to reduce the constraint on the time steps, which are 6 and 180 s for the barotropic and baroclinic modes, respectively. The vertical and horizontal viscosity (and diffusion) coefficients are flow-dependent according to the level 2.5 turbulence closure model of Mellor and Yamada [1982] and the formulation of Smagorinsky [1963], respectively. The horizontal diffusion coefficients are small (typically  $<10 \text{ m}^2 \text{ s}^{-1}$ ) throughout each simulation considered in this study.

[11] The alongshore boundary conditions are periodic for all variables. Consistent with this condition, an  $f$ -plane approximation is used, with  $f = 1.037 \times 10^{-4} \text{ s}^{-1}$ . In addition, the across-shore topographic section off Coos Bay ( $43.3^\circ\text{N}$ ), near the southern extent of the domain, is interpolated over 10 alongshore grid cells to match the

across-shore section off Tillamook Bay ( $45.6^\circ\text{N}$ ), near the northern extent of the domain, so that the topography is periodic in the  $y$ -direction. The use of periodic boundary conditions establishes a well-posed and robust model, but has its limitations. For example the model cannot represent net alongshore pressure gradients that might result from large scale, alongshore density gradients. Additionally, periodic boundary conditions force the modeled flow at the northern and southern extent of the domain to be equal. With these limitations noted, we find that this configuration is capable of reproducing a substantial fraction of the observed variance in the region of interest [Oke et al., 2002a]. Additionally, it provides a good testing ground for research into coastal data assimilation which is very much in its infancy.

[12] The offshore boundary conditions are zero gradient for the tangential velocities and elevation  $\eta$ , a modified radiation condition for the normal velocities [e.g., Chapman, 1985], and an upstream advection condition for the potential temperature  $\theta$  and salinity  $S$  [Blumberg and Kantha, 1985]. Comparisons of simulations run with the offshore boundary open and with it closed by a vertical wall indicate that the model solution on the shelf is insensitive to these conditions. Simulations with the open boundary conditions were spatially smoother however, presumably due to the reduced reflection of inertia-gravity waves. A partial slip condition is applied for the alongshore velocities at the coastal boundary. The alongshore component of the applied wind stress is calculated from time-varying winds measured at Newport, Oregon, and is assumed to be spatially uniform. To reduce the excitation of inertial oscillations the wind is low-pass filtered with a 40-hour half-amplitude filter. No surface heat flux is included in this study.

[13] The initial velocity field is at rest and the initial fields of  $\theta$  and  $S$  are horizontally uniform, with vertical profiles taken from the mean observed profiles during July 1973 at a station approximately 120 km offshore of Yaquina Head ( $44.65^\circ\text{N}$ ). The experiments discussed in sections 3 and 5 are spun up by applying observed winds for 10 days.

### 3. Model-Data Comparisons

[14] In order to assess whether the present model configuration is capable of adequately representing the dominant physical processes of the wind-driven shelf circulation off Oregon, a 3-month simulation is performed for the summer of 1998, and is compared with CODAR and ADP observations available for that time. All observed and model results are low-pass filtered with a 40-hour half-amplitude filter. Some model-data comparisons with the CODAR data are summarized in Figure 3. For those comparisons the CODAR data are linearly interpolated from the original data locations, with horizontal resolution of approximately 1 km, onto a subset of the horizontal model grid. It should be noted that only a representative subset of the observations (Figure 2) are used in the assimilation experiments presented in section 5. Mean fields of surface  $\mathbf{v}^m$  and  $\mathbf{v}^o$  (superscripts  $m$  and  $o$  denote model-only and observations, respectively) are shown in panels a and b, respectively. This comparison indicates that the spatial structure of the mean surface  $\mathbf{v}^m$  and  $\mathbf{v}^o$  are qualitatively similar, but there is a

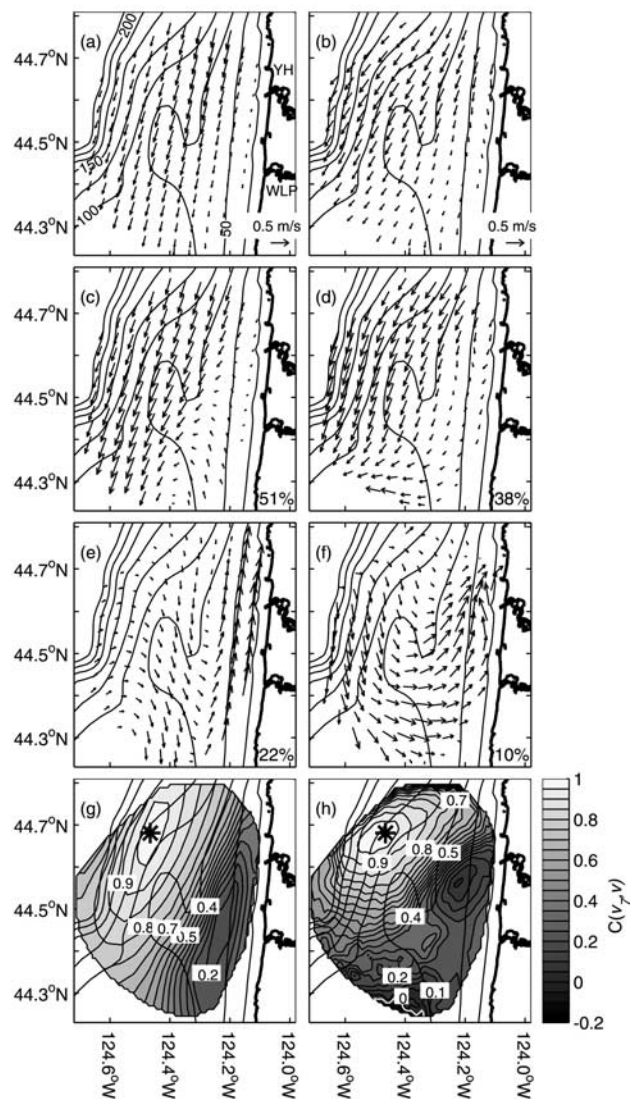


**Figure 3.** (left) Modeled and (right) observed mean surface velocity fields (a, b); mode 1 EOF (c, d); higher order EOF (e, f). The percent variance explained by each EOF is displayed in the lower right-hand corners. Cross-correlations between  $v_7$  at location 7 (location indicated by the star) and elsewhere (g, h).

general difference in the direction of the flow, with  $\mathbf{v}^o$  exhibiting a more dominant cross-isobath component. Also, the magnitude of  $\mathbf{v}^m$  is slightly less than  $\mathbf{v}^o$ . The dominant fluctuations in the surface  $\mathbf{v}^m$  and  $\mathbf{v}^o$  are represented by the mode 1 EOF (panels c and d) that represents fluctuations in the strength of the coastal jet. Higher order EOFs (Figures 3e and 3f) represent the structure of the flow associated with upwelling relaxation [Oke et al., 2002b]. These EOFs combined represent 73% and 48% of the modeled and observed variance, respectively. These comparisons demonstrate that the model is capable of reproducing fluctuations of the coastal jet and upwelling relaxation that are in qualitative agreement with observed fields. Cross-correlations between  $v_7$  (location 7) and the surface  $v$  elsewhere in

the CODAR region are shown for the model and the observations (Figures 3g and 3h). These cross-correlation fields are similar to elements used to define to forecast error covariance matrix in section 4.4. This comparison demonstrates that the modeled and observed cross-correlation fields have similar characteristics with high values in the direction of the coastal jet. Both cross-correlation fields also indicate that the decorrelation length scales are longer in the  $y$ -direction than in the  $x$ -direction. There is clearly a difference in the alignment of the maximum cross-correlations that is related to the above-mentioned differences in the direction of the surface velocities.

[15] In order to assess the model's performance at depth, the dominant EOFs from a vertical profile  $\mathbf{v}^o$  from a moored ADP located at 124.3°W and 44.65°N (Figure 2) are compared to the EOFs of  $\mathbf{v}^m$  (Figure 4). The first, second, and third modes of the EOFs from the model and the observations are qualitatively similar. For this comparison the first mode represents the dominant, alongshore barotropic motion, the second mode represents the dominant vertically sheared across-shore motion, and the third appears to represent a baroclinic mode. Again, while details differ, such as the depth of the zero crossing of the baroclinic mode, in general this comparison is favorable.

[16] An additional assessment of the model at depth is obtained by comparing the cross-correlation profiles of velocity over the water column with the velocity at a fixed

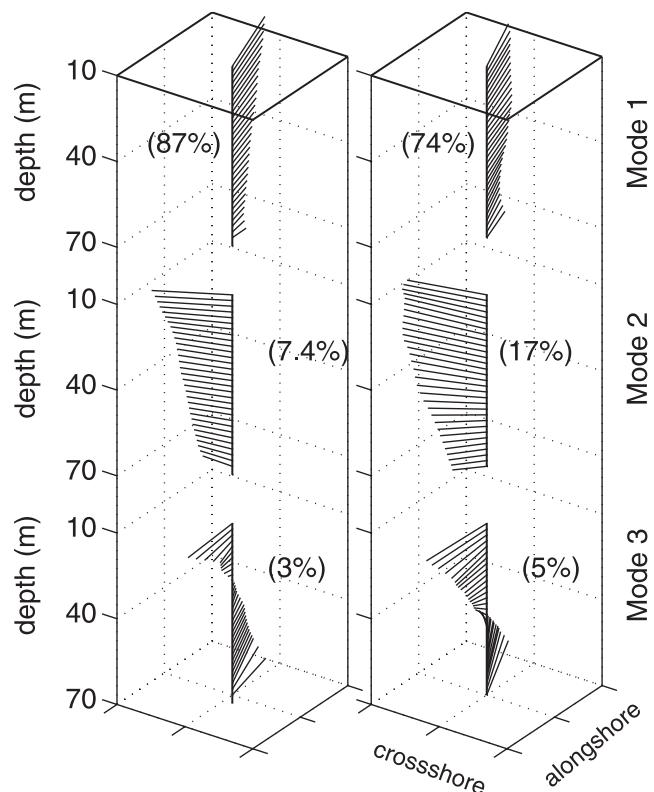


**Figure 4.** Dominant EOFs from a profile of velocity at 80 m depth from (left) the model results and from (right) a moored ADP for summer 1998. The percent variance explained by each EOF is indicated.

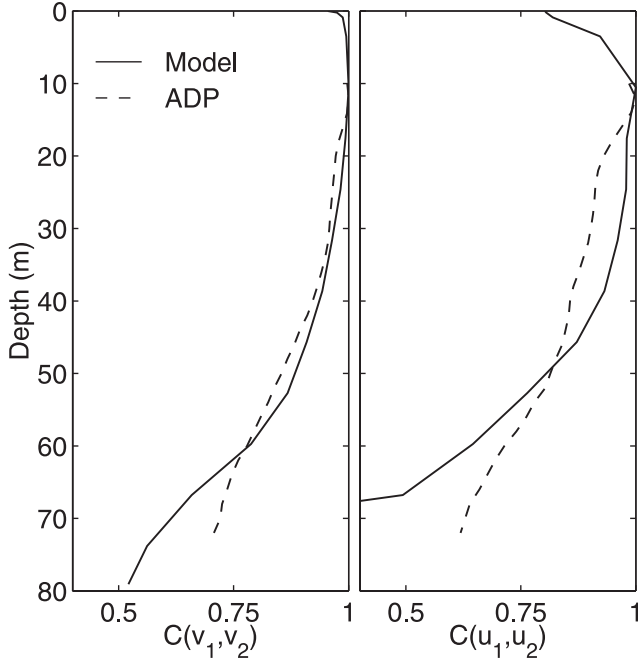


**Figure 5.** Cross-correlations between ADP velocities at 12 m depth with ADP velocities over the rest of the water column for the (left)  $v$  and (right)  $u$  components (dashed lines). Also shown are corresponding correlations between model velocities at 12 m depth and model velocities at other depths (solid lines).

point (12 m depth) from the model and from the ADP (Figure 5). Again, these fields are similar to elements used to formulate the forecast error covariances in section 4.4. The results indicate that the magnitude and vertical structure of the cross-correlations obtained from the model results are in good agreement with observations.

[17] The model-data comparisons presented in this section demonstrate that the model is able to qualitatively represent observed features of the shelf circulation. On the other hand, we recognize that certain physical effects are not included in the model configuration, such as the effects of surface heating that can be important during upwelling [e.g., *Federik and Allen, 1995*], the influence of the Columbia River plume that can be important as far south as Newport, or spatial variability in the wind [e.g., *Samelson et al., 2002*]. The sensitivity of this configuration to each of these factors is investigated in detail by *Oke et al. [2002a]*. In section 5 we show that the assimilation of surface velocity data enables the DAS to give a quantitatively improved representation of the coastal circulation.

## 4. Data Assimilation System

### 4.1. Analysis Equations

[18] The analysis equations that are based on Kalman filter theory [e.g., *Miller, 1986; Cohn and Parrish, 1991*], relate the analysis  $\mathbf{w}^a$  of the model state that consists of the prognostic variables ( $u$   $v$   $\theta$   $S$   $U$   $V$   $\eta$ ) at all horizontal grid locations at all depths to the model forecast  $\mathbf{w}^f$  and the observations  $\mathbf{w}^o$ . For this application the size of the model

state is  $n = \mathcal{O}(10^6)$ , and the number of observations is  $p = 18$ . The analysis equations are given by

$$\mathbf{w}^a = \mathbf{w}^f + \mathbf{K}\delta\mathbf{w} \quad (1)$$

$$\mathbf{K} = \mathbf{P}^f \mathbf{H}^T (\mathbf{H} \mathbf{P}^f \mathbf{H}^T + \mathbf{R})^{-1}, \quad (2)$$

where  $\mathbf{K}$  is the gain matrix ( $n \times p$ ),  $\delta\mathbf{w} = (\mathbf{w}^o - \mathbf{H}\mathbf{w}^f)$  is the innovation vector ( $p \times 1$ ),  $\mathbf{H}$  is a matrix that interpolates from the model space to the observation space ( $p \times n$ ),  $\mathbf{P}^f$  is the forecast error covariance matrix ( $n \times n$ ),  $\mathbf{R}$  is the observation error covariance matrix ( $p \times p$ ), and the superscript  $T$  denotes transpose. The innovation covariance matrix  $\mathbf{M}$  ( $p \times p$ ) is given by

$$\mathbf{M} = \mathbf{H} \mathbf{P}^f \mathbf{H}^T + \mathbf{R}. \quad (3)$$

[19] The gain matrix  $\mathbf{K}$  is used to extrapolate information from the observation sites onto the model domain. When the full Kalman Filter is implemented,  $\mathbf{P}^f$  is refined by updating it after each assimilation step using the model forecast and knowledge of the error characteristics of the dynamical equations [e.g., *Miller, 1986*]. Typically, after a long enough integration time  $\mathbf{P}^f$  reaches a state of equilibrium, denoted by  $\mathbf{P}^f_\infty$ . However, the computational cost of integrating  $\mathbf{P}^f$  is very high. For this study we have not implemented the full Kalman filter. We have assumed that our initial estimate of  $\mathbf{P}^f$  is approximately equal to  $\mathbf{P}^f_\infty$ , which we derive empirically, as described in section 4.4, and test for consistency through a series of objective statistical tests as described in Appendices B and C.

[20] At each assimilation step,  $u$ ,  $v$ ,  $\theta$ , and  $S$  are explicitly adjusted at all grid points. It is important to adjust  $U$ ,  $V$ , and  $\eta$  in a manner that is consistent with the model formulation and the adjustments to  $u$  and  $v$ . Details of this aspect of the implementation are described in Appendix A.

### 4.2. Eigenvalue Decomposition (EVD) Approach

[21] For most of the assimilation experiments that are presented in this study an eigenvalue decomposition (EVD) of the innovation covariance matrix

$$\mathbf{M} = \mathbf{U}\mathbf{\Lambda}\mathbf{U}^T \quad (4)$$

is utilized. The columns of  $\mathbf{U}$  represent the eigenvectors of the innovation covariance matrix and the diagonals of  $\mathbf{\Lambda}$  are the corresponding eigenvalues. It follows from equation (4) that

$$\mathbf{M}^{-1} = \mathbf{U}\mathbf{\Lambda}^{-1}\mathbf{U}^T \quad (5)$$

because  $\mathbf{U}$  is orthonormal. In most experiments considered in this study  $\mathbf{U}$  and  $\mathbf{\Lambda}$  are truncated so that  $\mathbf{M}$  is approximated by  $\hat{\mathbf{M}}$  ( $p \times p$ ):

$$\hat{\mathbf{M}} = \hat{\mathbf{U}}\hat{\mathbf{\Lambda}}\hat{\mathbf{U}}^T, \quad (6)$$

where  $\hat{\mathbf{U}}$  ( $p \times m$ ) contains only the  $m$  (where  $m \leq p$ ) dominant orthogonal modes of  $\mathbf{M}$  and the diagonals of  $\hat{\mathbf{\Lambda}}$  ( $m \times m$ ) are the  $m$  largest eigenvalues. For the experiments discussed in section 5 where  $p = 18$ , when the number of

modes used in  $\hat{\mathbf{U}}$  are 1, 6, 12, and 18, approximately 50%, 90%, 98%, and 100% of the total variance of the original innovations is represented. For the EVD approach, equations (1) and (2) are solved in three steps:

$$\begin{aligned} \text{step 1 : } \delta\hat{\mathbf{w}} &= \hat{\mathbf{U}}^T \delta\mathbf{w}, \\ \text{step 2 : } \hat{\mathbf{y}} &= \hat{\mathbf{\Lambda}}^{-1} \delta\hat{\mathbf{w}}, \\ \text{step 3 : } \mathbf{w}^a &= \mathbf{w}^f + \mathbf{P}^f \mathbf{H}^T \hat{\mathbf{U}} \hat{\mathbf{y}}. \end{aligned} \quad (7)$$

Step 1 projects the innovations onto the dominant orthogonal modes of  $\mathbf{M}$ , where  $\delta\hat{\mathbf{w}}$  ( $m \times 1$ ) represents the spatially filtered innovation. In step 2,  $\hat{\mathbf{y}}$  ( $m \times 1$ ) is obtained through a simple scalar division of  $\delta\hat{\mathbf{w}}$  by the eigenvalues of the dominant modes. The analysis of the model state  $\mathbf{w}^a$  is calculated in step 3. The analysis is then used as the initial conditions for the start of the next assimilation cycle. A discussion on the justification for the EVD approach is presented in section 4.6, after the formulation of  $\mathbf{P}^f$  and  $\mathbf{R}$  is described.

### 4.3. Time-Distributed Averaging Procedure (TDAP)

[22] There are two practical difficulties to overcome when assimilating velocity data into a primitive equation model. The first issue is that of data compatibility. For studies of wind-driven circulation the velocity measurements are low-pass filtered with a 40-hour half-amplitude filter prior to assimilation in order to eliminate the energetic tidal signals and high frequency fluctuations that are not of primary interest. The primitive equation model, however, contains physics that allows fluctuations at all frequencies. Therefore an assimilation procedure that combines the low-pass filtered observations with the unfiltered model forecast to produce  $\delta\mathbf{w}$  would involve comparing two incompatible data sources. This problem is overcome by low-pass filtering the model forecast. The second issue is that of initialization. Simply stated, primitive equation models are sensitive to discontinuous changes in their model fields [e.g., *Smedstad and Fox, 1994*]. This sensitivity typically triggers an artificial adjustment process that involves a shock-like response of the model fields to these changes resulting in high frequency oscillations that may grow in amplitude. Consequently, the quality of the subsequent assimilation may be reduced. This difficulty is overcome by gradually introducing the corrections over time. Alternative strategies for overcoming the problem of initialization include damped time-differencing schemes [e.g., *Baker et al., 1987*], initialization methods [e.g., *Lynch and Huang, 1992*], explicit balance constraints [e.g., *Parrish and Derber, 1992*] and nudging [e.g., *Stauffer and Seaman, 1990*; *Smedstad and Fox, 1994*; *Lewis et al., 1998*]. While each of these strategies are effective for initialization, none of them deal with the problem of data compatibility.

[23] A practical solution to the issues of data compatibility and initialization outlined above is a TDAP, represented schematically in Figure 6. Beginning with the model initial conditions at time  $t = 0$ , the model is integrated forward to  $t = T/4$ , where  $T$  is an inertial period ( $\approx 17$  hours) and the full model state, required for a “seamless restart,” is stored. The model is then integrated to  $t = T$  and the time

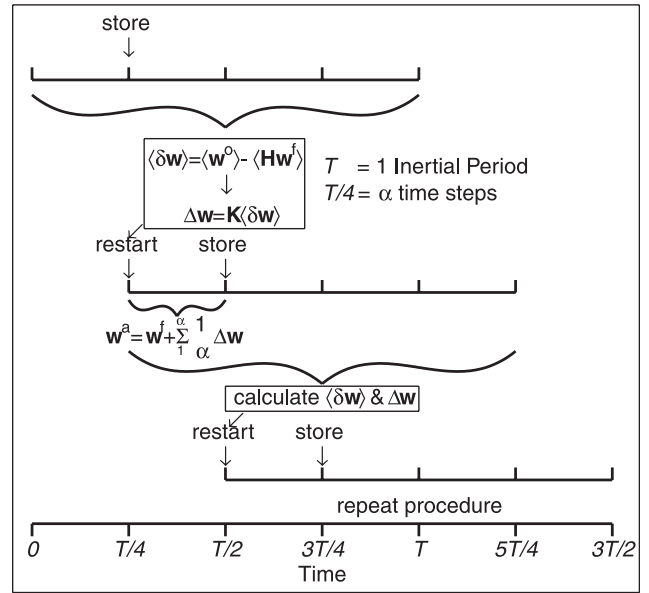


**Figure 6.** Schematic representation of the TDAP described in section 4 where  $\langle \rangle$  in the figure are the same as  $\langle \rangle_T$  in equations (8) and (9) and denote a time average over an inertial period,  $T$ .

averaged forecast  $\langle \mathbf{H}\mathbf{w}^f \rangle_T$  (where  $\langle \rangle$  denotes a time average over  $T$ ), centered at  $t = T/2$ , is calculated. The low-pass filtered observations  $\langle \mathbf{w}^o \rangle_T$  at  $t = T/2$  and the inertially averaged forecast  $\langle \mathbf{H}\mathbf{w}^f \rangle_T$  are then differenced,

$$\langle \delta\mathbf{w} \rangle = \langle \mathbf{w}^o \rangle - \langle \mathbf{H}\mathbf{w}^f \rangle_T, \quad (8)$$

and applied to the analysis equations where the correction

$$\Delta\mathbf{w} = \mathbf{K}(\delta\mathbf{w})_T \quad (9)$$

is calculated and stored. The model is then restarted at  $t = T/4$ , with the full model state that was previously stored, and the correction is imposed over a quarter of an inertial period by adding a fraction  $1/\alpha$  (where  $\alpha$  is the number of time steps in the interval  $T/4$ ) of the correction to the model at each time step,

$$\mathbf{w}^a = \mathbf{w}^f + \sum_{1/\alpha} \Delta\mathbf{w}, \quad (10)$$

so that at  $t = T/2$  the full correction  $\Delta\mathbf{w}$  has been added. At  $t = T/2$  the full model state is again stored and the model is integrated forward to  $t = 5T/4$  where the inertial average centered at  $t = 3T/4$  is evaluated and the analysis for the next assimilation cycle is calculated. The TDAP is then repeated for subsequent assimilation cycles.

[24] This procedure can be derived by including the time-averaging in  $\mathbf{H}$ . However, implementing the procedure in that way requires storage of the state vector for multiple time steps, which would be computationally more expensive than the approach that we utilize here.

[25] The computational cost of implementing the TDAP is equivalent to four model runs in addition to the cost of solving the analysis equations. Since we want to resolve all

subinertial frequencies, in order to reduce the effects of aliasing of near-inertial fluctuations a conservative timescale for each assimilation cycle is  $T/4$ . Although, the frequency response of the box car filter (time average) used in the TDAP is not ideal [e.g., *Smith*, 1997], it is demonstrated in section 5 that the benefits of employing this simple filter are much greater than any negative influence that may result as a consequence of its poor frequency response. A linear analysis of the incremental updating procedure [*Bloom et al.*, 1996] that is very similar to the time-distributing component of the TDAP showed that the primary effect of the time-distribution is to act as a low-pass filter on the system's response to the introduced adjustments. This is confirmed in section 5 by comparing the power spectra of assimilation results with and without TDAP.

#### 4.4. Forecast Error Model

[26] The most challenging aspect of sequential data assimilation is the estimation of  $\mathbf{P}^f$ . Note that in practice, only the columns of  $\mathbf{P}^f$  that relate the forecast errors at the observation sites to the rest of the model domain need to be estimated and stored, since  $\mathbf{P}^f$  never appears alone in equations (1), (2) and (3), but always as  $\mathbf{P}^f \mathbf{H}^T$ . This is of practical significance since it reduces the storage of an  $n \times n$  matrix  $\mathbf{P}^f$  to that of a  $n \times p$  matrix  $\mathbf{P}^f \mathbf{H}^T$ . Similarly, for the EVD approach only the  $n \times m$  matrix  $\mathbf{P}^f \mathbf{H}^T \hat{\mathbf{U}}$  needs to be stored for the assimilation. Many applications of data assimilation in oceanography and meteorology have involved the assumptions that  $\mathbf{P}^f$  is homogeneous and isotropic in space and stationary in time [e.g., *Rutherford*, 1972; *Rienecker and Miller*, 1991; *Bartello and Mitchell*, 1992; *Chen and Wang*, 1999]. Although such assumptions may be appropriate for the open ocean, they would seem to be inappropriate for applications to the coastal ocean.

[27] To avoid these strong assumptions, we have begun by assuming that  $\mathbf{P}^f$  is proportional to the typical cross-correlations between the model variables. This enables a physically consistent inhomogeneous and anisotropic estimate of  $\mathbf{P}^f$  to be estimated using an ensemble of typical summer simulations, forced with observed winds from Newport, Oregon. The rationale behind this approach is that if two elements of the state are typically correlated, then their forecast errors are also likely to be correlated. More explicitly, we have formulated  $\mathbf{P}^f$  in terms of the standard deviations  $\sigma_w^m$  ( $n \times 1$ ) obtained from a 40-day model-only simulation for the full assimilation period (superscript  $m$  denotes model-only) and an empirically derived universal (and stationary in time) correlation function  $\mathbf{C}$  ( $n \times p$ ). An element of  $\mathbf{P}^f$  is given by

$$P_{ij}^f = \sigma_{w_i}^E \sigma_{w_j}^m C_{ij}, \quad (11)$$

where  $\sigma_{w_i}^E = \gamma_i \sigma_{w_i}^m$  is the effective standard deviation of  $w_i$  and  $C_{ij} = C(w_i, w_j)$  is the cross-correlation between  $w_i$  and  $w_j$  averaged over the ensemble of 18 summers. The parameter  $\gamma_i = 0.5$  when  $\sigma_{w_i}^m$  corresponds to  $\theta$  or  $S$  (denoted by  $\gamma_i^{0.5}$ ) and is 1.0 otherwise. We found that reducing the standard deviation of  $\theta^m$  and  $S^m$  in equation (11) by 50% ( $\gamma_i^{0.5} = 0.5$ ) significantly improved the comparisons between the analyzed subsurface velocity fields with observed velocities at the ADP site. The cross-correlations between modeled variables for each year  $C(w_i, w_j)$  are calculated (with the

time mean for that year subtracted) in the usual way. Although the forcing winds are spatially constant there are a number of effective degrees of freedom in every ensemble run due to the time variability of the wind. Thus the rank of  $\mathbf{M}$  is sufficient for assimilation experiments where 18 independent observations are assimilated. Since only  $\mathbf{P}^f \mathbf{H}^T$  is used in the assimilation,  $P_{ij}^f$  is only calculated for  $i = 1 \dots n$  and  $j = 1 \dots p$ , where the selected  $j$  indices correspond to the velocity components at the observation sites.

[28] Elements of  $\mathbf{C}$  are similar to the cross-correlation fields presented in Figures 3 and 5. The positive model-data comparisons presented in those figures give us reason to believe that the dependence of  $\mathbf{P}^f$  on  $\mathbf{C}$  is reasonable. Note that the standard deviations  $\sigma_w^m$  of the model state are derived from a model-only simulation for the particular year, season or event of interest and are used to scale  $\mathbf{C}$ , providing a quasi-nonstationary estimate for  $\mathbf{P}^f$ . Also note that, although this formulation appears to assume that the magnitude of the forecast error is comparable to the magnitude of the signal, in fact it is the ratio of  $\mathbf{H} \mathbf{P}^f \mathbf{H}^T$  to  $\mathbf{R}$  in equation (2) that is important.

[29] The structure of the columns of  $\mathbf{C}$  provide insight into the nature of the summer upwelling circulation off Oregon throughout the model domain. The correlation fields also contain information about the decorrelation length scales and the anisotropic nature of the correlation fields used in the formulation of  $\mathbf{P}^f$ . The standard error of the averages of  $\mathbf{C}$  are typically less than 0.05 indicating that the estimated ensemble average of the cross-correlations is a good representation of the typical cross-correlation between modeled fields. An example of fields from  $\mathbf{C}$  giving correlations between  $v_6$  (location 6; see Figure 2) and  $u$ ,  $v$ , and  $\theta$  at the surface are shown in Figure 7. The  $C(v_6, u)$  fields indicate that when  $v_6$  is southwards,  $u$  at the surface is typically offshore in the vicinity of location 6 and shoreward to the south of Heceta Bank. The offshore flow is consistent with wind-driven upwelling and the shoreward flow demonstrates the importance of the local topography in steering the coastal jet on the Oregon shelf. The plot of  $C(v_6, v)$  indicates that the coastal jet is most coherent in the  $y$ -direction to the north of location 6 and is less coherent on the shoreward side to the south of location 6. This feature is due to the tendency for a northward counter current to develop on the shoreward side of the coastal jet between  $44^\circ\text{N}$  and  $44.7^\circ\text{N}$  during periods of upwelling relaxation [*Oke et al.*, 2002b]. The fields of  $C(v_6, \theta)$  indicate that the fluctuations in  $\theta$  are well correlated with the fluctuations in the coastal jet, as indicated by the high cross-correlations ( $>0.8$ ) on the shoreward side of location 6. This field also indicates that  $\theta$  to the south of Heceta Bank is typically not well correlated with  $v_6$ .

#### 4.5. Observation Error Model

[30] Previous experience with HF radar data in other regions demonstrates that HF radar derived velocities are not error free, and that low-pass filtering improves the correspondence between CODAR surface velocities and near-surface measurements obtained from moored instruments [*Paduan and Rosenfield*, 1996]. The HF radar data we use is spatially averaged in the transformation from pairs of nonorthogonal radial vectors to vectors in a fixed ( $u, v$ ) coordinate system. Therefore, the observation error is likely

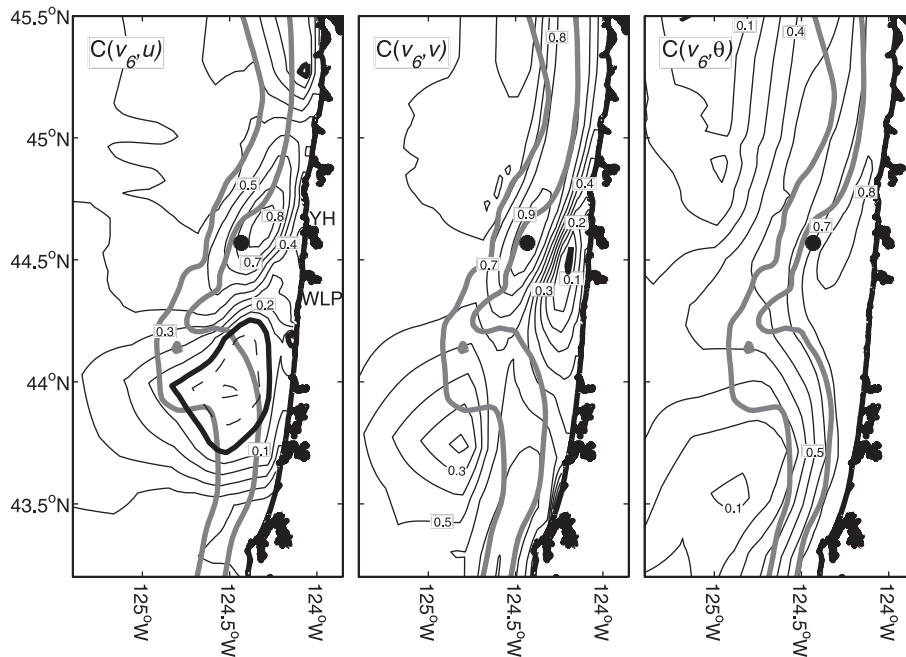


**Figure 7.** Universal cross-correlations between alongshore velocity  $v_6$  at location 6, denoted by the asterisk, and (left) the across-shore velocity  $u$ , (middle) alongshore velocity  $v$  and (right) temperature  $\theta$  at the surface (contour interval = 0.1; thick line, zero; dashed line, negative).

to be spatially correlated in a manner that depends in a complex way on the length scales used in this transformation as well as the angle of intersection of the radial beams, even if errors in the raw radial velocities are uncorrelated. Given that many of the factors that cause errors in the CODAR measurements (such as environmental factors or errors in determining the azimuth of received signals) are likely to effect multiple radial velocities in a similar way, it is unlikely that the correlation structure in even the raw data is so simple. We therefore expect data errors to have a complicated correlation structure with length scales perhaps only slightly shorter than the correlation length scales of the signal. We implement this idea in an admittedly approximate fashion by assuming that  $\mathbf{R}$  is proportional to the covariances of the observations (signal plus noise) themselves,

$$\mathbf{R} = \beta \langle \mathbf{w}^o \mathbf{w}^{oT} \rangle, \quad (12)$$

where  $\langle \rangle$  denotes a time average over the 40-day analysis period. Here  $\beta$  is a constant that determines the relative magnitude of  $\mathbf{H}\mathbf{P}^f\mathbf{H}^T$  and  $\mathbf{R}$  in equation (2). In the assimilation experiments that are presented in section 5,  $\beta$  is varied while elements of  $\mathbf{P}^f$  are held constant, in order to determine the most appropriate estimate for  $\mathbf{R}$  relative to  $\mathbf{H}\mathbf{P}^f\mathbf{H}^T$ . As we discuss below, our model for  $\mathbf{R}$  is almost certainly not quite correct. However, we believe this is more reasonable than a simple isotropic uncorrelated model ( $\mathbf{R} = s^2\mathbf{I}$ ). Further efforts to understand error structure in HF radar derived data are clearly warranted.

#### 4.6. Justification for the Truncation of $\mathbf{M}$

[31] There are small-scale variations in the observations that cannot adequately be represented by the model due to limited resolution and numerical noise. Inclusion of these variations results in a local correction that introduces a

dynamical imbalance that can cause spurious high-frequency oscillations. It is therefore essential to reduce these small-scale features and noise in the data prior to assimilation. Adding  $\mathbf{R}$  to  $\mathbf{H}\mathbf{P}\mathbf{H}^T$  to form the innovation error covariance  $\mathbf{M}$  should in principle accomplish this. As demonstrated in Figures 3g and 3h the modeled surface velocity fields have longer length scales than the corresponding observed fields. The effect of smaller spatial scale components of the observed fields on the analysis should thus be expected to be relatively reduced when  $\delta\mathbf{w}$  is multiplied by  $\mathbf{M}^{-1}$ . However, computation of the condition number of  $\mathbf{R}$  reveals that this matrix is almost as poorly conditioned as  $\mathbf{H}\mathbf{P}\mathbf{H}^T$ , leaving some possible short spatial scale features in the data relatively undamped. These features must occur only rarely, since eigenvectors of  $\mathbf{R}$  associated with small eigenvalues correspond to directions in the data space with very small variance. However, contamination of the assimilation by even rare short spatial scale perturbations may be expected to degrade the performance of the DAS, and it is best to avoid this possibility. By truncating  $\mathbf{M}$  we retain only the realistic components of the observed velocities to produce the analysis. The value of this approach is demonstrated in section 5 where the experiments with six modes are shown to give better results than those with 12 and 18 modes.

[32] The EVD approach is standard in data assimilation [e.g., Bennett, 1985; Parker, 1994] and it has many practical benefits. Bennett [1985] noted that in numerical experiments utilizing an EVD approach and truncating the low eigenvalue modes, as described in section 4.2, performed better than damping with a diagonal  $\mathbf{R}$ , especially when the observations are not error free. Additionally, the EVD is less computationally expensive and will allow for a larger number of data to be assimilated more efficiently at a smaller computational cost, although this benefit has not

been exploited in this study. Furthermore, when low eigenvalue modes of  $\mathbf{M}$  are truncated, the performance of the DAS is less sensitive to misspecification of  $\mathbf{R}$ . This is clearly a major concern here, where we have had to essentially guess a plausible form for the error covariance.

[33] The eigenvalue spectrum of the innovation matrix provides an indication of how many independent measurements can be extracted from the CODAR array. We find that the innovations are best represented by six modes, representing approximately 90% of the total variance, suggesting that there are only six independent measurements in the CODAR array that we are utilizing here.

[34] One additional comment is in order on our use of the EVD approach. In the canonical case where the error covariance is taken to be isotropic ( $\mathbf{R} = s^2\mathbf{I}$ ), the EVD is normally performed on  $\mathbf{HPH}^T$ . With the more complex form for  $\mathbf{R}$  assumed here, the standard theory [e.g., Parker, 1994] suggests that the EVD truncation should be applied to the transformed problem, obtained by multiplying data and data functionals by the matrix  $\mathbf{R}^{-1/2}$ . Although this approach should be optimal if our model for  $\mathbf{R}$  were exactly correct, the transformation is unstable in our case, since  $\mathbf{R}$  is itself relatively poorly conditioned. We have thus applied the EVD to  $\mathbf{M}$ , and verified through analysis of the resulting data space projections that the way the truncation is constructed has very little effect on the large scale signal component.

#### 4.7. Limitations of the Data Assimilation System

[35] In section 5, the success of the DAS is demonstrated through a detailed hindcast study. Here we note that the details of this system may require adaptations if one is to apply it to other more complicated regions (e.g., complex topography and canyons). Clearly, by nature of the assimilation process, the analyzed results are strongly dependent on the structure of  $\mathbf{P}^f\mathbf{H}^T$ . Therefore, appropriate estimation of  $\mathbf{P}^f\mathbf{H}^T$  is crucial to the system's success. Application to the Oregon continental shelf is simplified by the prevalence of predictable, coherent modes of variability of the flow fields during the upwelling season, with dominant modes relating to wind-driven upwelling (Figures 3c and 3d) and relaxation from upwelling (Figures 3e and 3f). As a result, estimates of  $\mathbf{P}^f\mathbf{H}^T$  that have realistic inhomogeneous and anisotropic structures can be obtained using the relatively simple approach outlined in section 4.4. For other more complicated situations a state dependent version of  $\mathbf{P}^f\mathbf{H}^T$  may be required.

[36] Another limitation of this DAS is the choice of ensemble members used to formulate  $\mathbf{P}^f\mathbf{H}^T$ . For simplicity, we have limited our ensemble to 18 simulations with spatially uniform wind stress, no surface heating, and no river forcing, using only one set of initial conditions. Clearly, by including ensemble members with variations to these factors, a more complete ensemble could be established. This approach would also increase the rank of  $\mathbf{HP}^f\mathbf{H}^T$  and might enable a greater number of independent observations to be assimilated. In section 5 we find that the DAS works best when only six modes, representing approximately 90% of  $\mathbf{M}$ , are used following the method described in section 4.2. We interpret this as an indication that there are only 6 independent measurements in the CODAR array. However, additional variability in

**Table 1.** Summary of Assimilation Experiments Where  $\beta$  Determines the Magnitude of  $\mathbf{R}$  According to Equation 12<sup>a</sup>

Experiment	Description		
1	no assimilation	(model-only)	
2–4	$\beta = 0.4, 1.0, 1.6;$	no TDAP,	EVD 6 modes
5–7	$\beta = 0.4, 1.0, 1.6;$	TDAP,	no EVD
8–10	$\beta = 0.4, 1.0, 1.6;$	TDAP,	EVD 12 modes
11–20	$\beta = 0.05, 0.1, 0.2,$ $0.4, \dots, 1.6;$	TDAP,	EVD 6 modes
21–23	$\beta = 0.4, 1.0, 1.6;$	TDAP,	EVD 1 mode
24	exp. 14, $T_I = T/2$		
25	exp. 14, $T_I = T$		
26	exp. 14, no-wind		
27	exp. 14, persistence		

<sup>a</sup>EVD and TDAP refer to different implementations of the assimilation scheme described in section 4; the assimilation time interval  $T_I = T/4$ , where  $T$  is an inertial period ( $\approx 17$  hours), in all of the assimilation experiments except experiments 24 and 25.

the data might be accommodated by a more complete set of model forcing errors.

## 5. Assimilation of HF Radar Data

### 5.1. Validation of Analysis

[37] The effectiveness of the DAS described in section 4 is demonstrated through a series of assimilation experiments for the summer of 1998. Each experiment uses 18 data (9  $u, v$  pairs) at each assimilation time from the locations indicated in Figure 2. Experiments are performed using 1, 6, 12, and 18 modes in  $\hat{\mathbf{M}}$  (equation (6)) in order to test the hypothesis that the small-scale features that are inadequately supported by the model are projected onto the higher modes. Similarly experiments are run with and without the TDAP and with different values for  $\beta$  in equation (12). The details of the experiments are summarized in Table 1. The control experiment for this study is experiment 1 (model-only), which is a 40-day model run after the initial spin-up for the summer of 1998 without assimilation. Over this period the mean value of the alongshore wind stress was  $-0.0084$  Pa with a standard deviation of 0.026 Pa. The performance of each assimilation run is evaluated by comparing analyzed subsurface velocities with observations from the moored ADP (Figure 2). The ADP data are not used in the assimilation procedure. The ADP provides subsurface measurements of  $u$  and  $v$  at vertical spacings of 4 m between depths of 12 and 72 m. The results from the experiments are compared to the results from experiment 1 in order to assess the benefit of each assimilation.

[38] In order to objectively compare the modeled, analyzed, and observed vector fields the mean and standard deviation of the magnitude of  $\mathbf{V}$ ,  $\langle (U^2 + V^2)^{0.5} \rangle$ , and  $\sigma_{(U^2+V^2)^{0.5}}$ , respectively, are considered, where  $\langle \rangle$  denotes a time average over the 40-day analysis period. Also the magnitude of the complex cross-correlation coefficients  $\rho^*$  and the phase angles  $\theta^*$  [Kundu, 1976] between the  $\mathbf{V}^o$  and  $\mathbf{V}^m$  or  $\mathbf{V}^a$  are calculated. The value of  $\rho^*$  is independent of the coordinate system of the vector fields and  $\theta^*$  is the average counterclockwise angle of  $\mathbf{V}^m$  or  $\mathbf{V}^a$  with respect to  $\mathbf{V}^o$ , and is only meaningful if  $\rho^*$  is significant. The estimated 95% significance level for  $\rho^*$  is 0.51 that is determined using standard statistical techniques [e.g., Brunk, 1965].

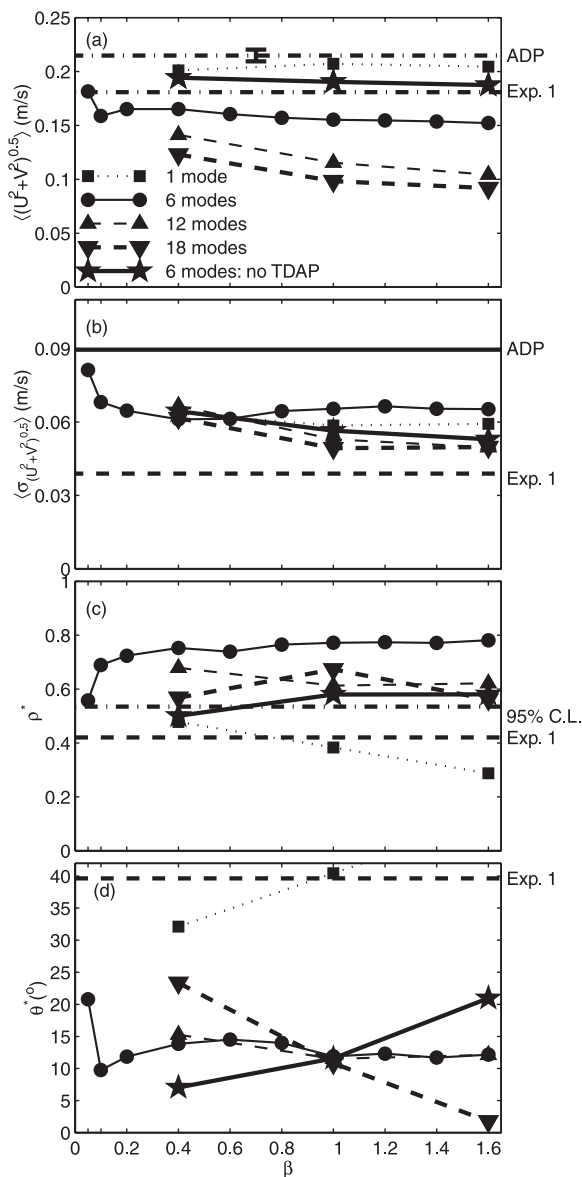


**Figure 8.** Assessment of the analyzed depth-averaged velocities at the ADP site showing (a)  $\langle(U^2 + V^2)^{0.5}\rangle$ ; (b)  $\sigma_{(U^2 + V^2)^{0.5}}$ ; (c)  $\rho^*$ ; and (d)  $\theta^*$  for assimilation experiments 2–23 with various number of modes used in equation (6) and for different values of  $\beta$  in equation (12) (Table 1). Results from each experiment are represented by a single dot in each panel and experiments with the same number of modes are joined according to the legend in Figure 8a. The ADP and model-only experiment 1 values are shown on the right of each panel.

[39] These statistical comparisons are presented in Figure 8 for experiments 2–23. For the ADP observations,  $\langle(U^2 + V^2)^{0.5}\rangle$  is  $0.21 \text{ m s}^{-1}$  and  $\sigma_{(U^2 + V^2)^{0.5}}$  is  $0.09 \text{ m s}^{-1}$ . In contrast,  $\langle(U^2 + V^2)^{0.5}\rangle$  and  $\sigma_{(U^2 + V^2)^{0.5}}$  from the model-only experiment are  $0.18$  and  $0.049 \text{ m s}^{-1}$ , respectively. For most of the assimilation experiments  $\langle(U^2 + V^2)^{0.5}\rangle$  is less than both the observations and the model-only results, indicating that there is a bias in the DAS with the magnitudes of the analyzed velocities typically  $0.05 \text{ m s}^{-1}$  less than those observed. The reason for this bias is unclear.

However, as discussed in Appendix C, there is no significant bias in  $\delta\hat{\mathbf{w}}$ . In the assimilation experiments  $\sigma_{(U^2 + V^2)^{0.5}}$  is less than the deviations in the observations and greater than the deviations in the model-only solution. This indicates that one effect of the assimilation is to increase the magnitude of the fluctuations of the velocity field so that they are in better agreement with the observations.

[40] For the model-only experiment,  $\rho^* = 0.42$ , which is below the estimated 95% significance level. In order to determine whether the EVD approach outlined in section 4 is beneficial, and to determine the most appropriate number of modes that should be used in this decomposition, assimilation experiments are performed with various values for  $\beta$  (0.4, 1.0, and 1.6) in equation (12) using 1, 6, 12, and 18 modes of  $\hat{\mathbf{M}}$  in equation (6). The results (Figure 8) indicate that for most of these assimilation experiments  $\rho^*$  is above the 95% significance level for each value of  $\beta$ . Furthermore, the experiments that used six modes and the TDAP had the highest correlations. This result indicates that the contributions of the forecast and observation errors to the innovations are smallest when the innovations are projected onto only six modes. This suggests that our assumption that the error covariance satisfies equation (12) is not completely correct. This also demonstrates the value of the EVD approach in making the assimilation procedure more robust to violations of our a priori covariance assumptions.

[41] The benefit of the TDAP is demonstrated by comparing the results in Figure 8 for experiments 2–4 (no TDAP) with experiments 14, 17, and 20 (Table 1). A comparison of the energy preserving spectra of the principal component of  $\mathbf{V}$  for assimilation experiment 14, with and without TDAP (without TDAP denoted by  $\mathbf{V}^{a*}$ ), from the model-only experiment and from the observations at the ADP location (Figure 9) further demonstrates the benefit of the TDAP. The spectrum of the assimilation without TDAP shows much greater energy in the high-frequency regime around the inertial frequency 1.5 cycles-per-day (cpd). Note that for the frequencies of interest ( $<0.4$  cpd) the spectrum from experiment 14 typically lies between that of the observations and the model-only results, as we expect.

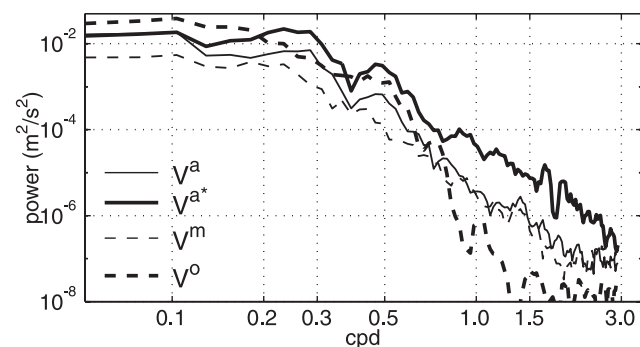


**Figure 9.** The energy preserving spectrum of the principal component of  $\mathbf{V}$  at the ADP location (denoted in Figure 2). The superscripts  $a$ ,  $a^*$ ,  $m$ , and  $o$  denote assimilation (experiment 14), assimilation with no TDAP (experiment 2), model-only (experiment 1), and observation, respectively.

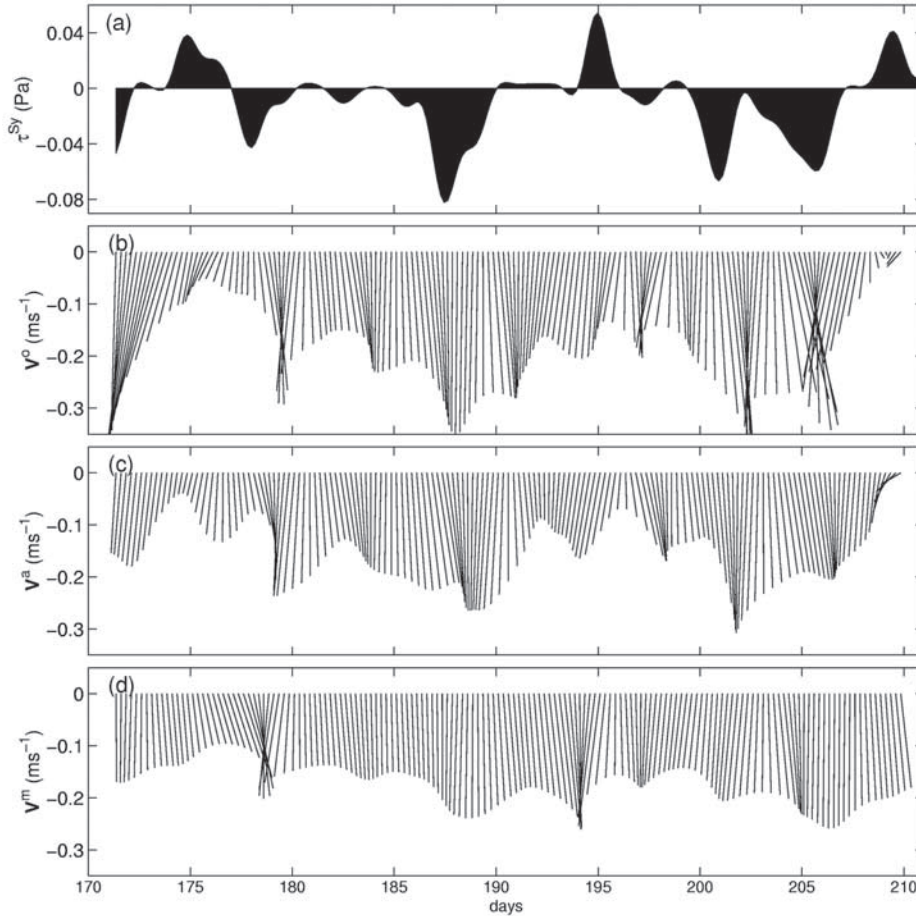


**Figure 10.** (a) The alongshore wind stress near Newport. Vector stick plots of  $\mathbf{V}$  from (b) the moored ADP, (c) assimilation experiment 14 ( $\beta = 0.4$ , six modes), and (d) model-only experiment 1 for the summer of 1998.

[42] Since the experiments with six modes that utilized the TDAP performed the best, additional experiments 11–20 with different values of  $\beta$  (0.05, 0.1, 0.2, 0.4, ..., 1.6) were performed with six modes in order to assess the effects of changing the relative magnitudes of  $\mathbf{P}^f$  and  $\mathbf{R}$ . Interestingly, out of experiments 11–20, all of which used six modes, the experiment with  $\beta = 0.05$  performed the worst, and as  $\beta$  increased  $\rho^*$  increased to a maximum of about 0.78 for  $\beta \geq 0.4$ . For the model-only experiment,  $\theta^* = 40^\circ$  (although  $\rho^* < 95\%$  significant level), while  $\theta^*$  for most of the assimilation experiments are much less than this. For experiments 11–20 (six modes),  $\theta^* \approx 11^\circ$  for  $\beta \geq 0.4$ .

[43] In addition, a series of objective statistical tests designed to test the validity of  $\mathbf{P}^f$  and  $\mathbf{R}$  are performed on the innovation time series for each experiment. A description of these tests is presented in Appendix B and C along with the results. Briefly, these analyses demonstrate that the hypotheses about the prior error statistics cannot be rejected for experiments 14 and 15 when six modes are used with  $\beta = 0.4$  or 0.6. These tests also demonstrate that the variance of the innovations is reduced when six modes are used compared to when 12 modes or 18 modes (no EVD) are used.

[44] On the basis of the considerations described above, we conclude that the best analysis is produced by assim-

ilation experiment 14 with  $\beta = 0.4$  using six modes. Vector stick plots of  $\mathbf{V}^o$  from the ADP,  $\mathbf{V}^a$  from assimilation experiment 14 and  $\mathbf{V}^m$  from experiment 1 are compared in Figure 10. These plots indicate that many of the details of the fluctuations in  $\mathbf{V}^o$  are well represented in  $\mathbf{V}^a$ . For example, the fluctuations on days 184, 188, 194, 197, and 202 are well represented by experiment 14, but are poorly represented by  $\mathbf{V}^m$ . While some fluctuations in  $\mathbf{V}^a$  are not evident in  $\mathbf{V}^o$  (e.g., days 176 and 191), the details of  $\mathbf{V}^a$  are typically in better agreement with  $\mathbf{V}^o$  than the details of  $\mathbf{V}^m$ , as indicated by the statistical comparisons described above. The statistics  $\langle (u^2 + v^2)^{0.5} \rangle$ ,  $\sigma_{(u^2+v^2)^{0.5}}$ ,  $\rho^*$ , and  $\theta^*$  from experiments 1 and 14, are plotted as a function of depth in Figure 11. The improvement in  $\rho^*$ ,  $\theta^*$ , and  $\sigma_{(u^2+v^2)^{0.5}}$  from assimilation experiment 14 compared to experiment 1 is evident. These comparisons imply that information from the surface velocity data is reliably projected over depth at this location, as supported by the value of  $\rho^* > 0.8$  around 65 m depth. From Figure 11,  $\langle (u^2 + v^2)^{0.5} \rangle$  doesn't change as a result of assimilation as much as  $\sigma_{(u^2+v^2)^{0.5}}$ , indicating that the assimilation enhances variability. As mentioned above however, the mean values from experiments 1 and 14 are both less than the observations.

[45] In all of the assimilation experiments described above, the assimilation interval  $T_I = T/4$  where  $T$  is an inertial period

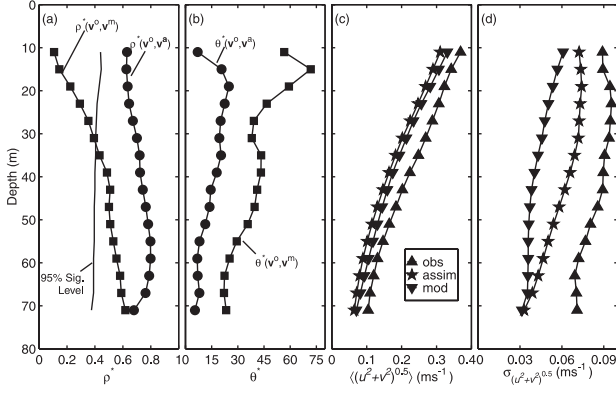


**Figure 11.** Plots of (a)  $\rho^*$ ; (b)  $\theta^*$ ; (c)  $\langle(u^2 + v^2)^{0.5}\rangle$ ; and (d)  $\sigma_{(u^2+v^2)^{0.5}}$  plotted as a function of depth for the ADP observations  $\mathbf{v}^o$ , the model-only experiment 1  $\mathbf{v}^m$  and assimilation experiment 14  $\mathbf{v}^a$ .

as described in section 4. In order to test the sensitivity of the results to  $T_I$  additional experiments were performed for  $\beta = 0.4$  using six modes with  $T_I = T/2$  and  $T_I = T$ , experiments 24 and 25, respectively. The analysis is in poorer agreement with the ADP velocities for these cases, with  $\rho^* = 0.65$  and  $\theta^* = 17^\circ$  for  $T_I = T/2$ , and  $\rho^* = 0.61$  and  $\theta^* = 20^\circ$  for  $T_I = T$ . Possibly a different value of  $\beta$  may be appropriate for these assimilation timescales.

[46] Additional assimilation experiments with  $\beta = 0.4$  using six modes were performed in order to test the sensitivity of the results to the choice of  $\gamma_i^{0S}$  in equation (11). Experiments with the above-mentioned elements of  $\gamma_i^{0S} = 1$  and 0 were performed and the comparisons with the ADP velocities showed that  $\rho^* = 0.48$  and  $\theta^* = 23^\circ$  for  $\gamma_i^{0S} = 1$  and  $\rho^* = 0.75$  and  $\theta^* = 5^\circ$  for  $\gamma_i^{0S} = 0$ . This result shows that an improved analysis is obtained when the density field is adjusted less, rather than more, and the analyzed velocity field is allowed to advectively adjust the density field during the time distribution of the adjustments.

[47] In order to further demonstrate the influence of the observations on the analyzed fields, a no-wind assimilation experiment (experiment 26), that is equivalent to experiment 14 with no wind forcing, is performed. This experiment is designed to give insight into the relative importance of the surface wind forcing and the forcing due to the assimilation. In addition, a series of persistence experiments [e.g., *Murphy*, 1992], where the dynamical model is not utilized, are performed in order to further test the validity of  $\mathbf{P}^f$ . A description of the persistence experiment is presented in Appendix D. A comparison between the resulting analyzed and observed depth-averaged velocities resulted in  $\rho^* = 0.74$  for the no-wind experiment and  $\rho^* = 0.7$  for the persistence experiment. These results demonstrate that in the vicinity of the ADP the forcing due to the assimilation is more important for the success of the DAS than the wind forcing, and that the error covariances used to project the surface velocities over depth at the ADP location are appropriate. For the assimilation experiments that did utilize the model and the wind forcing the highest value of  $\rho^* = 0.78$  is achieved. This represents only a minor improvement from the no-wind assimilation and persistence experiments. Beyond the range of influ-

ence of the assimilated observations, however, we expect the assimilation to perform better than the no-wind and persistence experiments.

## 5.2. Assessment of the Observing System

[48] Since the estimated observation and forecast error covariances satisfy the statistical tests outlined in Appendix C, an assessment of the relative contributions of the observations and the model to the analysis is appropriate. These relative contributions are determined by the relative magnitudes of  $\mathbf{HP}^f\mathbf{H}^T$  and  $\mathbf{R}$  that are used to formulate  $\mathbf{K}$  in equation (2). This idea can be understood by considering the diagonal elements of the reduced gain  $\mathbf{HK}$  that may be represented, approximately, for the  $k$ th element as

$$\mathbf{HK}_{kk} \approx \frac{\sigma_{\epsilon_k^f}^2}{\sigma_{\epsilon_k^f}^2 + \sigma_{\epsilon_k^o}^2}, \quad (13)$$

where  $\sigma_X^2$  is the variance of the scalar quantity  $X$ . The values of  $\mathbf{HK}_{kk}$  are indicative of the relative magnitudes of the forecast and observation errors,  $\epsilon_k^f$  and  $\epsilon_k^o$ , respectively. The ratio of model to observation that is used to produce the analysis therefore reflects these relative errors. When the EVD is used the innovations are spatially filtered by the dominant modes of  $\mathbf{M}$  prior to the assimilation. In that case,

$$\hat{\mathbf{H}}\mathbf{K} = \mathbf{HP}^f\mathbf{H}^T\hat{\mathbf{M}}^{-1} \quad (14)$$

determines the ratio of forecast to observation that is used to produce each analysis. Observations with a low signal to noise ratio are primarily represented by the higher modes of  $\mathbf{M}$ . These modes are omitted when the EVD approach is used and so observations with a low signal to noise ratio are not heavily weighted in step 1 of equation (7). If the  $k$ th observation is expected to have a low signal to noise ratio,  $\hat{\mathbf{H}}\mathbf{K}_{kk} \ll \mathbf{HK}_{kk}$ . The analysis at each observation location is approximately given by

$$w_k^a \approx [1 - \hat{\mathbf{H}}\mathbf{K}_{kk}]w_k^f + \hat{\mathbf{H}}\mathbf{K}_{kk}w_k^o. \quad (15)$$

[49] Elements  $\mathbf{HK}_{kk}$  and  $\hat{\mathbf{H}}\mathbf{K}_{kk}$  corresponding to the velocity components ( $u$ ,  $v$ ) at each observation location are displayed for experiment 14 in Figure 12. The mean of  $\mathbf{HK}_{kk} \times 100$  for ( $u$ ,  $v$ ) is (50,64) indicating that we expect  $u^o$  and  $u^f$  to have similar error variances. Similarly, we expect the typical errors of  $v^o$  to be less than  $v^f$ . The minimum in  $\mathbf{HK}_{kk}$  for  $u$ , corresponding to the maximum expected observation error, is adjacent to the coast where the angle of intersection of the radial beams from the CODAR transmitters are almost parallel. This is consistent with the expected limitations of the CODAR system in resolving both components of velocity [*Lipa and Barrick*, 1983; *Leise*, 1984].

[50] The fields of  $\hat{\mathbf{H}}\mathbf{K}_{kk}$  in Figure 12 (right panel) show the relative weights of the ( $u^o$ ,  $v^o$ ) and ( $u^f$ ,  $v^f$ ) that are used to produce ( $u^a$ ,  $v^a$ ) when six modes are used in the EVD of  $\mathbf{M}$ . A comparison at location 7 (Figure 2) shows  $\mathbf{HK}_{kk} \gg \hat{\mathbf{H}}\mathbf{K}_{kk}$ , which indicates that the observations at location 7 are primarily noise. Conversely,  $v^o$  at location 1, where  $\mathbf{HK}_{kk}$

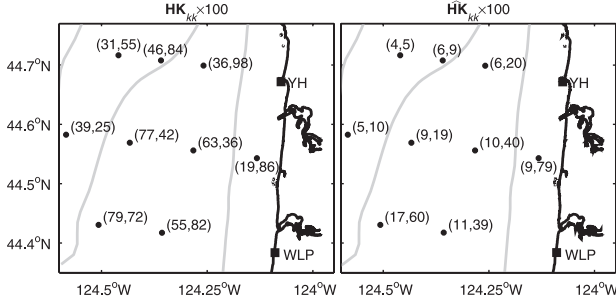


**Figure 12.** Elements of (left)  $\mathbf{HK}_{kk}$  and (right)  $\hat{\mathbf{HK}}_{kk}$  multiplied by 100 for each  $(u, v)$  pair for assimilation experiment 14. Each number represents the percent of  $(u_k^a, v_k^a)$  that was made up of  $(u_k^o, v_k^o)$  (e.g., when the EVD is used (right panel),  $u_1^a \approx 0.91u_1^o + 0.09u_1^f$  and  $v_1^a \approx 0.21v_1^o + 0.79v_1^f$ ).

$\approx \hat{\mathbf{HK}}_{kk}$ , consists mostly of a signal that is coherent with the other observations and is thus almost entirely represented by the dominant eigenvectors of  $\mathbf{M}$ . In general, Figure 12 indicates that when the EVD approach is used, the observations are typically not as heavily weighted compared to when no EVD is used. This is to be expected since the projection of the innovations onto the dominant modes of  $\mathbf{M}$  is a spatial filter of the original innovations.

[51] The average value of  $\hat{\mathbf{HK}}_{kk}$  indicates that the DAS performs most effectively when, on average, 80% of the analysis is made up of the model solution. This percentage is strongly dependent on the number of modes used in the assimilation (e.g., if 18 modes were used, only 43% of the analysis is made up of the model solution). This analysis provides an informative, but incomplete, measure of the relative contributions of the observations with respect to the forecast since each model forecast depends heavily on the previous analysis, which in turn depends on the observations. The temporal influence of a single datum can be better understood by considering an idealized, depth-averaged alongshore momentum equation where the acceleration depends only on wind forcing, linear bottom friction, and the assimilation:

$$V_t + \frac{rV}{h} = \frac{\tau^{Sy}}{\rho_0 h} + \Delta V^c, \quad (16)$$

where  $r$  is the bottom friction coefficient,  $h$  is the water depth,  $\rho_0$  is a reference density,  $\tau^{Sy}$  is the alongshore wind stress, and  $\Delta V^c$  is the depth average of  $\sum_{j=1}^p K_{ij} \delta w_j / \Delta t$ , which is the correction term where  $K_{ij}$  are the appropriate elements of the gain matrix. Integrating equation (16) [e.g., *Lentz and Winant, 1986*] shows that

$$V = \int_0^t \left( \frac{\tau^{Sy}}{\rho_0 h} + \Delta V^c \right) e^{-(t-s)/T_f} ds + V_0 e^{-(t-t_0)/T_f}, \quad (17)$$

where  $T_f = h/r$  is the frictional timescale that is approximately 4.5 days for the barotropic flow [e.g., *Brink and Allen, 1978*] and  $V_0$  is the initial velocity. This solution indicates that, just as the instantaneous wind stress affects the circulation for some time after it occurs, the correction at each assimilation cycle likewise affects the circulation over

similar timescales that are greater than the assimilation cycle ( $\approx 4$  hours). This indicates that the ratio of forecast to observation used to produce the analysis is not completely represented by  $\mathbf{HK}_{kk}$  or  $\hat{\mathbf{HK}}_{kk}$ .

## 6. Analysis

### 6.1. Analyzed Versus Modeled Fields

[52] The surface fields of  $\mathbf{v}$  and potential density  $\sigma_\theta$  produced by assimilation experiment 14, the model-only, the no-wind assimilation, and the persistence experiment (superscripts  $a$ ,  $m$ ,  $nw$ , and  $p$ , respectively) are presented in Figure 13. The fields from  $\mathbf{v}^a$ ,  $\mathbf{v}^{nw}$ , and  $\mathbf{v}^p$  show the coastal jet following the isobaths offshore as the continental shelf broadens over Heceta Bank (denoted in Figure 2). Also,  $\mathbf{v}^a$  and  $\mathbf{v}^{nw}$  show a cold-core meander located immediately to the south of Heceta Bank between the 100- and 200-m isobaths. The field of  $\mathbf{v}^m$  shows the coastal jet flowing southwards over the mid- to inner-shelf with minimal apparent effects of the topography. Additionally,  $\mathbf{v}^a$  shows the coastal jet separating near Newport, with the main jet flowing offshore, and a weaker jet continuing along the coast. The standard deviations of the surface velocity magnitudes show very high fluctuations in  $\mathbf{v}^a$  and  $\mathbf{v}^{nw}$ , and to a lesser extent  $\mathbf{v}^p$ , over Heceta Bank.

[53] The mean surface  $\sigma_\theta$  fields indicate that the amount of upwelled water at the surface is much greater for the assimilation experiments, with water that is denser than  $1024 \text{ kg m}^{-3}$  at the surface over Heceta Bank out to the 200-m isobath. Also, the assimilation experiments show that there is typically a dense pool of water between the 100- and 200-m isobaths near Heceta Bank. This dense pool of water corresponds to the cyclonic circulation in the surface velocity field. Recent hydrographic observations off Oregon [*Barth et al., 2001*] show the presence of such a feature during summer 1999. The model-only and persistence experiments show the upwelled water confined near the coast, and concentrated off Newport. Similarly, the  $\sigma_\theta$  fluctuations are much greater over Heceta Bank, and along most of the continental shelf for the assimilation experiments compared to the model-only solution and the persistence experiment. We find that in the persistence experiment increasing the effective standard deviations of  $\theta^m$  and  $S^m$ , by increasing  $\gamma_i$  from 0.5 to 1.0 in equation (11), gives a  $\sigma_\theta$  field that is closer to the analyzed  $\sigma_\theta$  from the assimilation experiment. However the comparison with the ADP observations are less favorable. This aspect of the error covariance estimates is investigated further below.

[54] The mean and standard deviations of  $\mathbf{v}$  and  $\sigma_\theta$  fields for an across-shore section over Heceta Bank ( $44.25^\circ\text{N}$ ) from assimilation experiment 14, the model-only, the no-wind assimilation, and the persistence experiments, are shown in Figure 14. The across-shelf section over Heceta Bank ( $44.25^\circ\text{N}$ ) is located immediately to the north of the dense pool of water discussed above and evident in Figure 13. The fields of  $\langle \mathbf{v}^a \rangle$ ,  $\langle \mathbf{v}^{nw} \rangle$ , and  $\langle \mathbf{v}^p \rangle$  show that the main coastal jet is located offshore, over the shelf break, with an area of weak northward flow over the mid-shelf that is associated with the eddy evident in the mean surface velocities (Figure 13). Also, there is evidence of a weak, southward jet adjacent to the coast. These fields demonstrate the separation of the coastal jet as discussed above. In

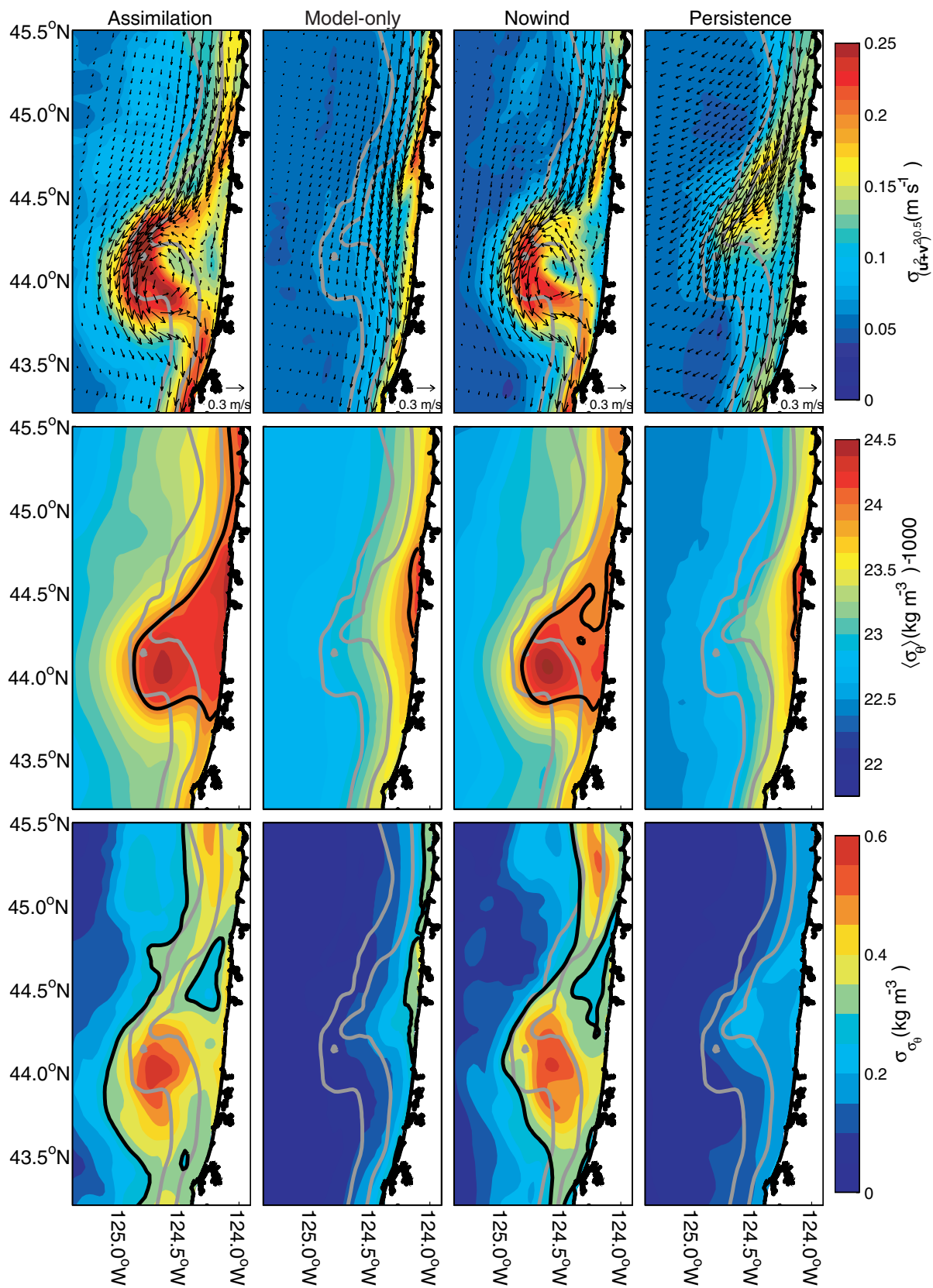


**Figure 13.** (top) Mean surface velocity vectors overlaying the standard deviation of the velocity magnitudes, (middle) mean surface  $\sigma_\theta$  (thick line,  $1024 \text{ kg m}^{-3}$ ), and (bottom) standard deviation of surface  $\sigma_\theta$  (thick line,  $0.3 \text{ kg m}^{-3}$ ) from (left to right) the assimilation experiment 14 ( $\beta = 0.4$ , six modes), model-only, no-wind, and persistence experiments. The 100- and 200-m isobaths are contoured in gray.

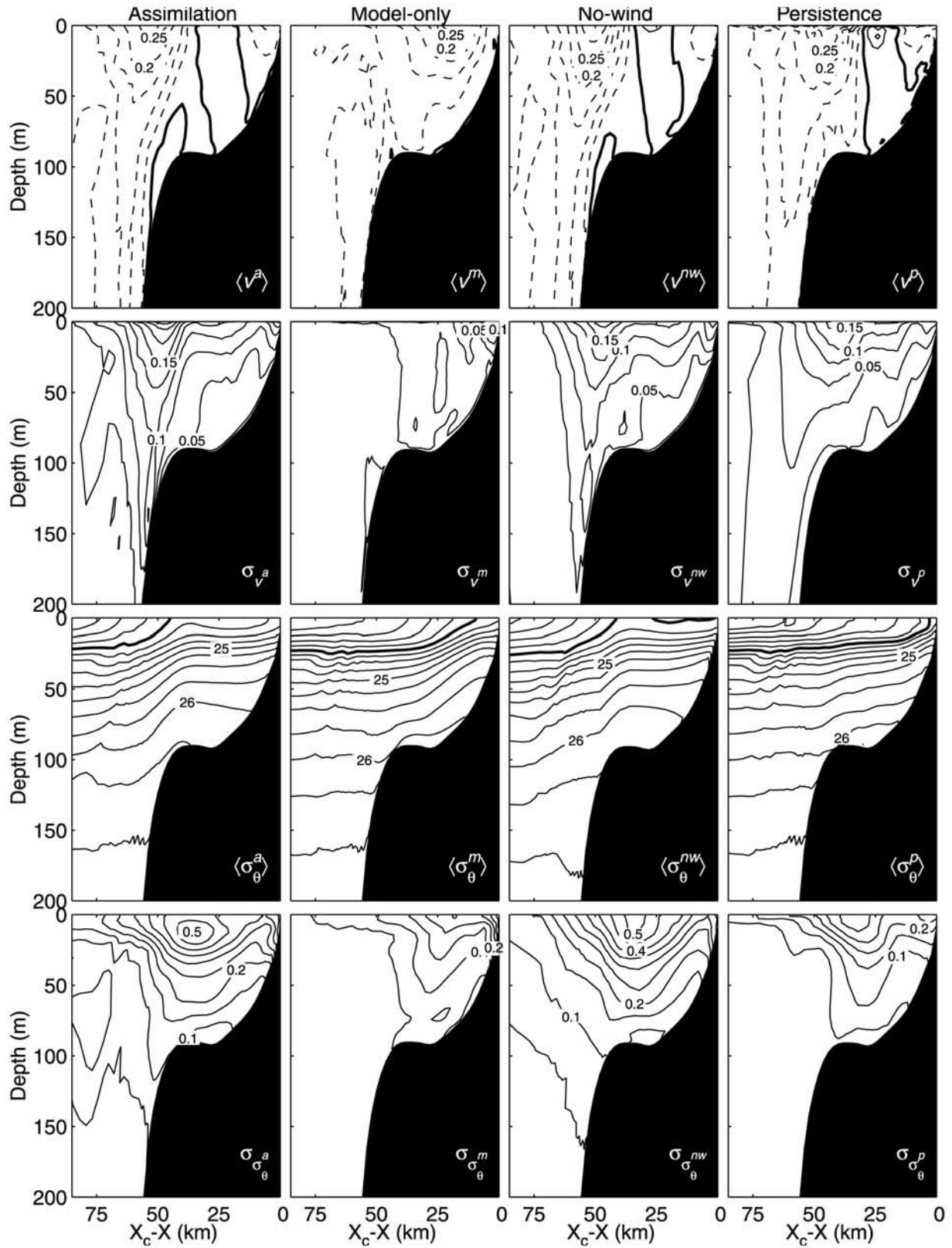


**Figure 14.** Fields of  $\langle v \rangle$  ( $\Delta v = 0.05 \text{ m s}^{-1}$ ; dashed line, southward; thick solid line, zero),  $\sigma_v$  ( $\Delta \sigma_v = 0.025 \text{ m s}^{-1}$ );  $\langle \sigma_\theta \rangle$  ( $\Delta \sigma_\theta = 0.25 \text{ kg m}^{-3}$ ; thick solid line,  $24 \text{ kg m}^{-3}$ ), and  $\sigma_{\sigma_\theta}$  ( $\Delta \sigma_\theta = 0.05 \text{ kg m}^{-3}$ ) from (left to right) the assimilation experiment 14, model-only, no-wind, and persistence experiments over Heceta Bank  $44.25^\circ\text{N}$ .

contrast,  $\langle v^m \rangle$  consists of a single, coherent coastal jet located over the mid- to inner-shelf. The fields of  $\sigma_{v^a}$  and  $\sigma_{v^m}$  are also very different over Heceta Bank. The analyzed fields have strong fluctuations over the shelf break, where the main coastal jet is located, while the model-only fluctuations are greatest near the coast. The field of  $\langle \sigma_{\theta}^a \rangle$  shows denser water outcropping over much of the shelf, while  $\langle \sigma_{\theta}^m \rangle$  and  $\langle \sigma_{\theta}^p \rangle$  show weaker upwelling concentrated near the coast. The field of  $\langle \sigma_{\theta}^{mv} \rangle$  is closer to that of  $\langle \sigma_{\theta}^a \rangle$  than  $\langle \sigma_{\theta}^m \rangle$ . This implies that the forcing due to assimilation has a larger impact than the wind forcing. The standard deviations of the  $\sigma_{\theta}$  fields again indicate greater fluctuations over a larger area in the assimilation experiment compared to the model-only experiment.

[55] As discussed in section 4.4 (Figure 7),  $C(v_6, v)$  are small to the south of Heceta Bank. However,  $v$  over Heceta Bank in the persistence experiment shows a region of northward flow below the surface (Figure 14), associated with the cyclonic meander evident in the surface fields of the assimilation and no-wind assimilation experiments in Figure 13. This feature is not evident in the surface fields from the persistence experiment in Figure 13 because the northward flow does not extend to the surface. Therefore the generation of the cyclonic meander is directly related to the assimilation. Apparently the observed currents in the CODAR array typically provide favorable conditions for this meander to be generated and maintained for most of the assimilation. Since the effect of the assimilation is to increase the magnitude of the fluctuations of the coastal jet locally around the sites of the CODAR observations, then the inertia of the stratified coastal jet might be causing it to cross contours of constant depth in the vicinity of Heceta Bank resulting in the generation of positive relative vorticity that may be contributing to the persistent cyclonic meander.

## 6.2. Depth-Averaged Alongshore Momentum Balance

[56] In the assimilation experiments the correction acts as a forcing on the right-hand side of the prognostic model equations. For the assimilation runs to be useful for investigating dynamical balances, the correction term should be small with respect to the other terms in the model equations. Alternatively, if the correction term does significantly contribute to the dynamical balances, then it would be useful if the nature of the correction term could be interpreted to help identify which term or terms in the model require correction.

[57] In order to investigate the role of the correction in the assimilation, we consider the term balances of the depth-averaged alongshore momentum equation ( $V$ -equation):

$$h^{-1}[(VD)_t + \mathbf{V} \cdot \nabla(VD) - F^y + fUD + DP_y \rho_0^{-1} - \tau^{Sy} \rho_0^{-1} + \tau^{By} \rho_0^{-1} - \Delta V^c D (2\Delta t^*)^{-1}] = 0, \quad (18)$$

where  $\nabla = \mathbf{i}\partial/\partial x + \mathbf{j}\partial/\partial y$ ;  $D = h + \eta$  where  $h$  is the water depth and  $\eta$  is the elevation;  $F^y = [(h2A_M V_y)_y + (hA_M(U_y + V_x))_x]$  is the horizontal viscosity term; subscripts  $x$ ,  $y$ , and  $t$  denote derivatives;  $f$  is the Coriolis parameter;  $P_y$  is the alongshore pressure gradient;  $\rho_0$  is a constant reference density;  $\tau^{Sy}$  and  $\tau^{By}$  are the alongshore components of the surface and bottom stress, respectively;  $\Delta V^c$  is the correction to  $V$ ; and  $\Delta t^*$  is the barotropic time step. The

mean and standard deviation of the terms in the  $V$ -equation are shown in Figure 15. The pressure gradient term and the Coriolis term are added together and presented as the ageostrophic term, in order to identify when the dynamical balances are significantly ageostrophic. Also, the advection term and the horizontal viscosity term are added together for conciseness. The horizontal viscosity term makes a negligible contribution to the dynamical balances, but is added so that the contribution of all terms is shown. Since the ageostrophic term is nonzero, we conclude that the alongshore momentum balance is ageostrophic as anticipated by typical scaling arguments [e.g., Allen, 1980]. Clearly, the dominant ageostrophic balance is between the ageostrophic term ( $h^{-1}[fUD + DP_y \rho_0^{-1}]$ ) and the nonlinear advection plus horizontal viscosity term ( $h^{-1}[\mathbf{V} \cdot \nabla(VD) - F_y]$ ), which have relatively high magnitudes in the means and standard deviations around Heceta Bank and adjacent to Newport. After these terms, the surface stress ( $-h^{-1}[\tau^{Sy} \rho_0^{-1}]$ ), bottom stress ( $h^{-1}[\tau^{By} \rho_0^{-1}]$ ), and correction ( $-h^{-1}[\Delta V^c D (2\Delta t^*)^{-1}]$ ) terms all have comparable magnitudes in the means. The standard deviations of the tendency ( $h^{-1}[(VD)_t]$ ) are similar in magnitude and structure to the standard deviations of the correction term.

[58] The effect on  $V$  of the correction term is to add a net southward (or northward) velocity when the correction term is positive (negative). In an area over the mid-shelf, between Yaquina Head and Waldport, the mean of the correction term is negative in the region of northward flow associated with the cold-core meander over Heceta Bank evident in Figure 13. Additionally, the correction term is positive over the inner-shelf adjacent to Newport, where the inner branch of the coastal jet is evident in the mean fields, and around the 100- and 200-m isobaths, where the main coastal jet is located in the assimilation experiment.

[59] The similarities in the magnitude and structure of the standard deviations of the tendency and correction terms suggests that the correction dominated the tendency, acting to adjust the modeled fields toward the analyzed state. This indicates that the contribution of the correction term is comparable to the other ageostrophic terms in the  $V$ -equation. Conversely, consideration of the term balances in the  $U$ -equation indicates that the dynamical balances are almost purely geostrophic. In addition, for the  $U$ -equation the contributions of the correction term are small compared to the ageostrophic terms in the equation that are themselves small compared to the geostrophic terms.

[60] If two terms in a model equation, with all terms on the same side, have a significant negative correlation, and if the magnitudes of both terms are comparable, one can conclude that there is a quasi-balance between them. This idea is applied to the alongshore momentum equation in order to determine whether the correction typically balanced or enhanced any of the terms in the momentum equation.

[61] Figure 16 shows a map of the cross-correlations between the correction and the terms in the  $V$ -equation. The results show a significant negative correlation between the correction term and the surface stress term adjacent to the coast. The sign of the correlation indicates that the correction typically acts to reduce the effective strength of the wind. The structure of this correlation field seems to suggest that the correction term is trying to introduce a curl in the wind stress near the coast. The effects of wind stress curl

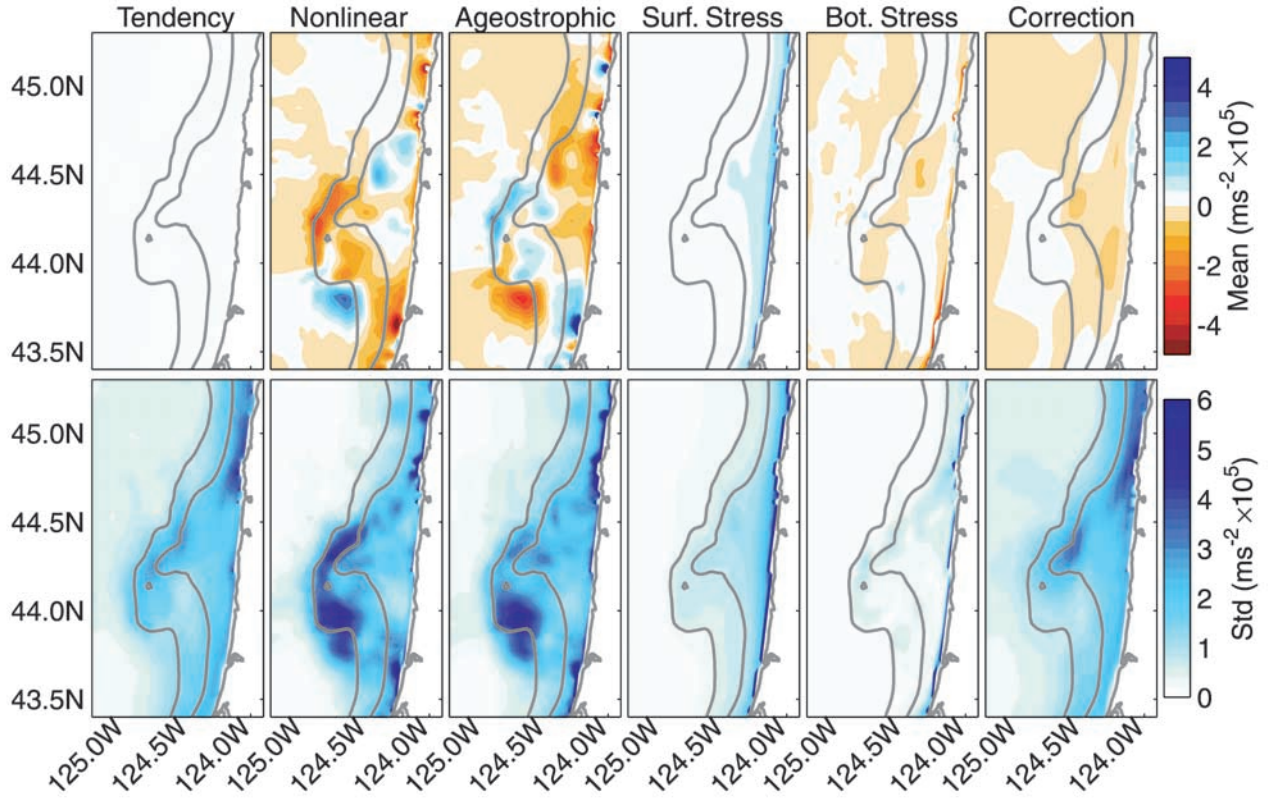


**Figure 15.** (top) Mean and (bottom) standard deviation of the terms in the  $V$ -equation (equation (18)) from assimilation experiment 14. The 100- and 200-m isobaths are plotted in gray.

on coastal upwelling have previously been documented [e.g., *Enriquez and Friehe, 1995*]. Notably, the region of high negative correlation between the correction term and the surface stress term corresponds to the region where the correction term is most dominant in the momentum balance with a high standard deviation (Figure 15). On the other hand it is possible that elsewhere in the domain a significant amount of the true wind stress is unrepresented by the applied wind stress field [e.g., *Samelson et al., 2002*], and because the

correction term has a weaker signal away from the coast, this analysis does not identify it as a significant source of error.

[62] In order to assess whether the claims that the assumption of spatially uniform wind is a source of model error, two additional experiments are performed. In both cases the spatial structure of the wind is objectively derived from the correlation between the surface stress and the correction term at every horizontal grid location  $C(SS, \Delta)$ . In case A the spatial structure of  $\tau^{5y}$  also depends on the

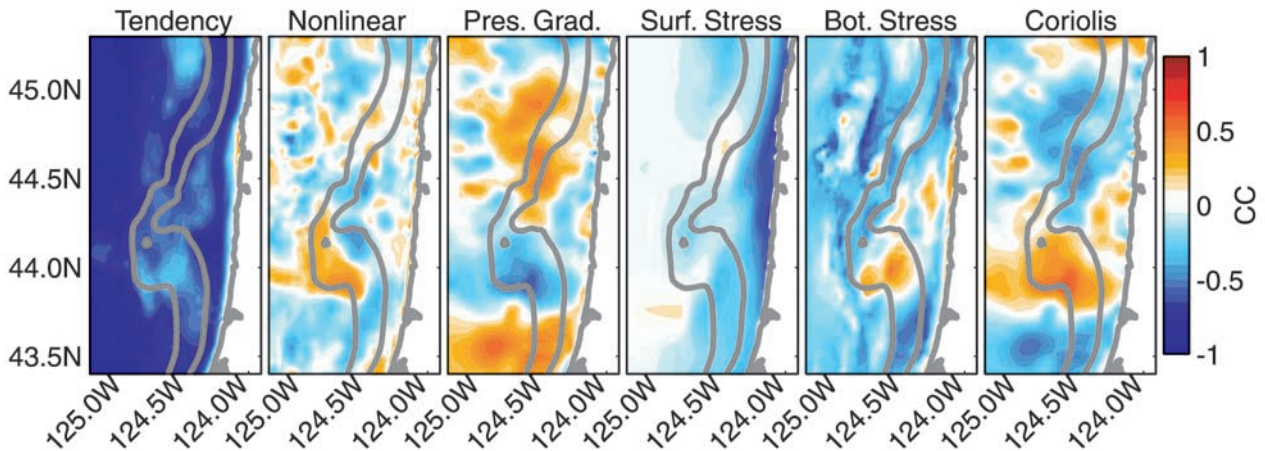


**Figure 16.** Cross-correlation fields between  $-\Delta V^c D(2\Delta t)^{-1}$  and the terms in the  $V$ -equation (equation (18)) from assimilation experiment 14. The 100- and 200-m isobaths are plotted.

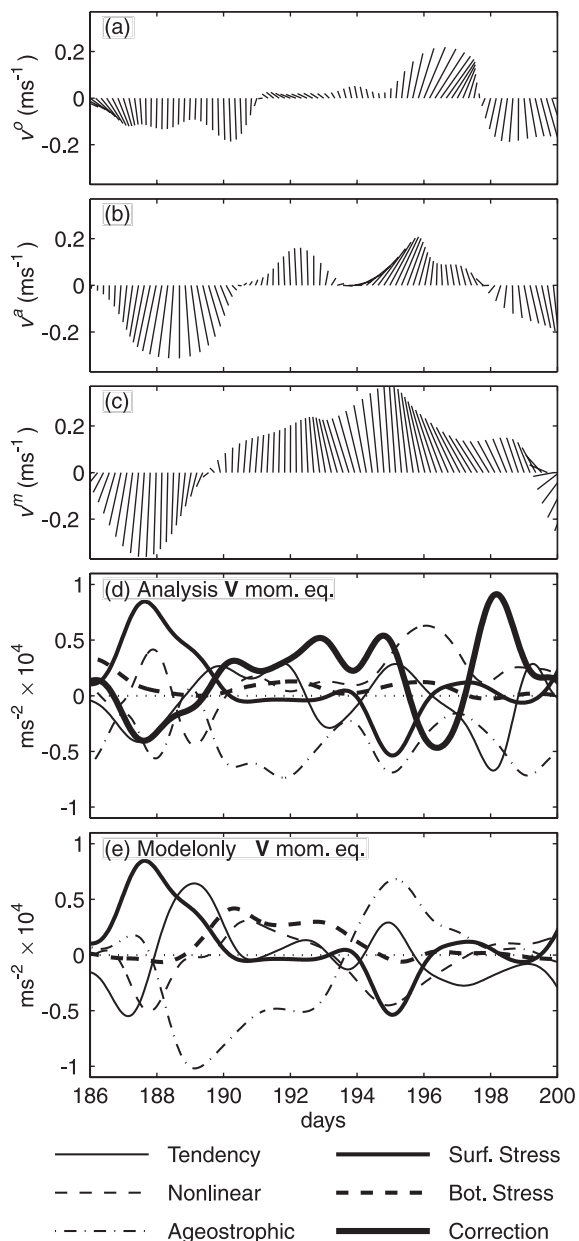


**Figure 17.** Time series of (a) observed, (b) analyzed, and (c) model-only surface velocity. Terms in the  $V$ -equation (equation (18)) from (d) assimilation experiment 14 and from (e) the model-only experiment at location 1 (see Figure 2).

standard deviation of the surface stress  $\sigma(S.S)$  and the correction  $\sigma(\Delta)$ :

$$\tau^{Sy}(x, y, t) = \tau^{Sy}(t) \left( 1 + C(SS, \Delta) \frac{\sigma(\Delta)}{\sigma(SS)} \right) \left( 1 + C(SS, \Delta) \frac{\sigma(\Delta)}{\sigma(SS)} \right)^{-1}, \quad (19)$$

where the subscript denotes evaluation at Newport. Here the structure function depends on  $x$  and  $y$  and is normalized by values at Newport because Newport is the only location where the true wind is observed. In case B,

$$\tau^{Sy}(x, t) = \tau^{Sy}(t) \left( 1 + \overline{C(SS, \Delta)^y} - \overline{C(SS, \Delta)^y} \right), \quad (20)$$

where  $\overline{C(SS, \Delta)^y}$  is the average of  $C(SS, \Delta)$  in the  $y$ -direction. The correlation field  $\overline{C(SS, \Delta)^y}$  is negative at the coast and approaches zero near the offshore boundary as indicated in Figure 16. The across-shore structure function in equation (20) is remarkably similar to the structure of the alongshore average of the first EOF of the modeled alongshore wind stress from a 3-month, high resolution simulation of the coastal atmosphere [Samelson *et al.*, 2002]. This function increases from 1 at the coast to a maximum of 1.75 near the offshore boundary with a structure that varies like  $\tau^{Sy}(x, t) = \tau^{Sy}(t) (1 + x^{0.5}/20)$ , where  $x$  is the distance offshore, in kilometers, from the coast.

[63] In both of the structure functions in equations (19) and (20) the applied wind stress at Newport is derived directly from observed winds, and the correction field from the assimilation experiment is used to objectively determine the spatial structure of the applied wind stress. The magnitude of the complex cross-correlation between modeled and observed  $\mathbf{V}$  for the model-only experiment is  $\rho^* = 0.42$ ; for case A it is  $\rho^* = 0.46$ ; and for case B it is  $\rho^* = 0.52$ . Both cases demonstrate a modest improvement confirming that the assumption that the wind is spatially uniform is a source of error. Clearly, there are other important model errors that are not addressed here including the lateral boundary conditions, as noted in section 2, initial conditions, and surface heating.

[64] The correlation between the correction term and the bottom stress term is negative to the north of Yaquina Head and south of Heceta Bank over the continental shelf. This relationship indicates that the correction acts to decrease the effective magnitude of the bottom stress fluctuations at these locations. The bottom stress could be overestimated if the magnitude of the bottom velocity is overestimated. This could occur if the baroclinic structure of the flow is inadequately represented.

[65] The correction term is significantly negatively correlated with the tendency term over most of the domain, which indicates that most of the correction is simply absorbed by the model tendency. This result suggests that even though the correction term is well correlated with the surface and bottom stress terms at some locations, the assimilation does not correct the inadequacies of these terms. Rather, the fluctuations of the correction term merely compensate for the inadequacies of these terms through corrections to the analyzed fields.

[66] Further insight into the role of the correction term is gained by considering a time series of the term balance of the  $V$ -equation. The time period between day 186 and 200 is considered because it demonstrates well the role of the correction term during a period in which the temporal variations in the wind forcing are significant. A time series of observed, analyzed (experiment 14), and model-only surface velocities, aligned in the direction of their principal axis, from location 1 (see Figure 2) over the inner-shelf, are shown in Figures 17a–17c. The analyzed velocity typically represents a combination of the observed and model-only velocity, as we would expect.

[67] It is clear from Figure 17d that the surface stress term is negatively correlated with the correction term, as already seen in Figure 16. Additionally, their average magnitudes are comparable during this time period. The correction term is typically acting to decrease the effective magnitude of the surface stress. As a result, the magnitude of the tendency is

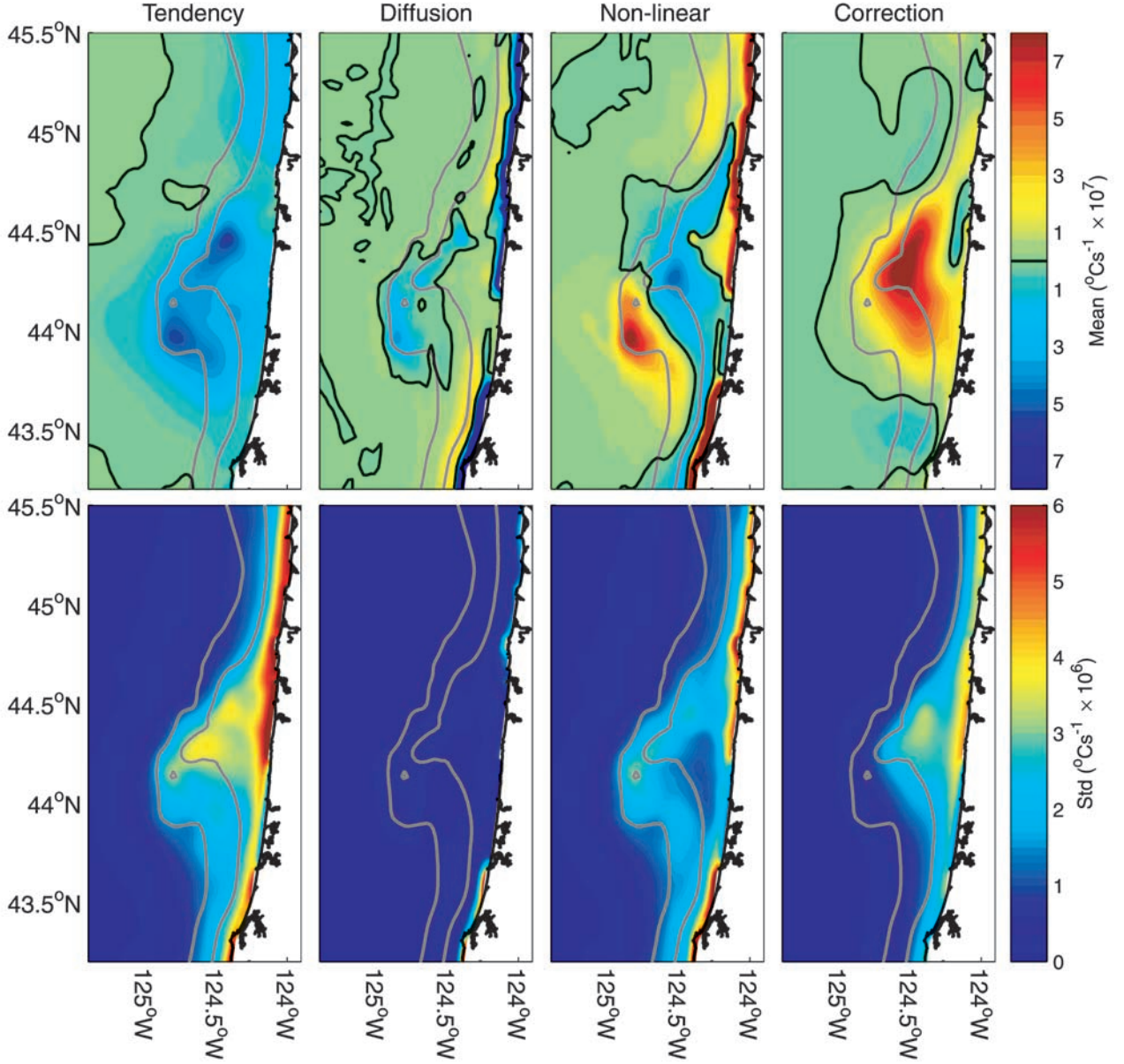


**Figure 18.** (top) Mean and (bottom) standard deviation of the depth-averaged terms in the  $\theta$ -equation (equation (21)) from assimilation experiment 14. The zero contour is highlighted (thick solid line) and the 100- and 200-m isobaths are plotted (gray).

reduced in the assimilation compared to the model-only experiment, and  $v^a$  is weaker than  $v^m$ . This analysis demonstrates how the correction term acts as a local forcing term during the assimilation.

### 6.3. Depth-Averaged Heat Balance

[68] The potential temperature equation ( $\theta$ -equation) is given by

$$(\theta D)_t + \mathbf{v}_3 \cdot \nabla_3 (\theta D) - (K_h D^{-1} \theta_z)_z - F^\theta - \Delta \theta^\circ D (2\Delta t)^{-1} = 0, \quad (21)$$

where  $\mathbf{v}_3$  is the velocity with components  $(u, v, w)$ , where  $w$  is the vertical velocity;  $\nabla_3 = \mathbf{i}\partial/\partial x + \mathbf{j}\partial/\partial y + \mathbf{k}\partial/\partial z$ ;  $F^\theta = (hA_h\theta_x)_x + (hA_h\theta_y)_y$  is the horizontal diffusion term and  $K_h$  and  $A_h$  are the vertical and horizontal diffusion coefficients,

respectively;  $\Delta \theta^\circ$  is the correction to  $\theta$  and  $\Delta t$  is the baroclinic time step. The depth-averaged mean and standard deviation of the terms in the  $\theta$ -equation are shown in Figure 18. An analogous analysis of the salinity equation yields similar results. In the discussion that follows, overbars denote a depth integral. In this study the depth-integral of the vertical diffusion  $(-h^{-1}(K_h D^{-1} \theta_z)_z)$  is zero due to the neglect of surface heating. Adjacent to the coast, to the north of  $44.2^\circ\text{N}$  and south of  $43.6^\circ\text{N}$  there is a local balance between the diffusion term  $(-h^{-1}[F^\theta])$  and the nonlinear term  $(h^{-1}[\mathbf{v}_3 \cdot \nabla_3 (\theta D)])$ , indicating that most of the upwelled water is diffused over the inner-shelf. The dominant terms over the mid- and outer-shelf are the tendency  $(h^{-1}[(\theta D)_t])$ , the correction term  $(-h^{-1}[\Delta \theta^\circ D (2\Delta t)^{-1}])$ , and the nonlinear term. The structure of the nonlinear term over Heceta Bank

reflects the structure of the mean surface velocities, with the change in sign reflecting the change in direction of the mean  $v$ . The nonlinear term is also important adjacent to the coast over much of the coastline representing a mean upwelling of isotherms in response to the local, upwelling favorable wind forcing. Where the correction term is positive the effect of assimilation is to decrease  $\theta$ . Clearly, the assimilation acted to decrease  $\theta$  over the shelf, effectively increasing the amount of upwelling, as demonstrated in Figure 13. The tendency is typically negative over the shelf, also consistent with a mean upwelling during the assimilation. By comparing the locations where the nonlinear and correction terms are high and positive, it is clear that the negative tendency is due to the correction term in the region where the surface velocities are assimilated (Figure 2) and that the nonlinear term additionally decreased  $\theta$  over the 200-m isobath beyond Heceta Bank. This feature of the term balance demonstrates how the nonlocal effects of the assimilation in the momentum equations, that strengthened the southward jet beyond Heceta Bank, adjusted the density field beyond the field of influence of the CODAR observations, as quantified in the universal correlation fields (e.g., see Figure 7, which shows that  $C(v_G, \theta)$  decreases to an insignificant level around the 200-m isobath to the south of Heceta Bank).

[69] The standard deviations of the terms in the  $\theta$ -equation indicate that the fluctuations of the tendency, nonlinear, and correction terms are high adjacent to the coast to the north of 44°N. Additionally, the standard deviation of the tendency and correction terms are also high over the mid-shelf in the region where CODAR data is assimilated. This suggests that much of the variations of the tendency are in response to the corrections. The nonlinear term also has a region of high standard deviation extending from the region where CODAR data is assimilated out to the 200-m isobath, beyond Heceta Bank. This is a region where the magnitude of the fluctuations of the coastal jet is increased in response to the assimilation (see Figure 13).

[70] The dominance of the correction term over the shelf demonstrates that, even when the effective standard deviations of  $\theta^m$  and  $S^m$  are reduced by choosing  $\gamma_i = 0.5$  in equation (11), the contributions of the assimilation to the  $\theta$ -equation are very significant. Efforts to find an optimal choice for  $\gamma$  were not fully pursued.

#### 6.4. Are the Adjustments in Geostrophic Balance?

[71] We find that in order to overcome the problem of initialization that results from imbalanced adjustments, the correction must be gradually introduced using the TDAP, enabling the model to further adjust the corrected fields. Scaling arguments for subinertial coastal fields imply that  $v$  should be in approximate geostrophic balance [e.g., *Allen et al.*, 1995]. In order to determine whether the adjusted  $v$ ,  $\sigma_\theta$ , and  $\eta$  are consistent with a geostrophic balance of  $v$ , the geostrophic velocities  $v_G$ ,

$$fv_G = g \frac{\partial \eta}{\partial x} + \frac{gD}{\rho_0} \int_{\sigma}^0 \left( \frac{\partial \sigma_\theta}{\partial x} - \frac{\sigma}{D} \frac{\partial D}{\partial x} \frac{\partial \sigma_\theta}{\partial \sigma} \right) d\sigma, \quad (22)$$

are calculated for assimilation experiment 14, the model-only, the no-wind assimilation, and the persistence experiments. Because  $\eta$  is not available for the persistence

experiment (see Appendices A and D),  $v_G$  is estimated in that case by vertically integrating the thermal wind relation referenced to  $v$  at mid-depth.

[72] Fields of  $\langle v \rangle$  are compared to  $\langle v_G \rangle$  in Figure 19 for the across-shore section over Heceta Bank near the dense pool of water (44.25°N) shown in Figure 13. Also plotted in Figure 19 are the mean ageostrophic velocities  $\langle v - v_G \rangle$  and the standard deviation of the ageostrophic velocities  $\sigma_{v-v_G}$ . The magnitudes of  $\langle v^m - v_G^m \rangle$  are typically between 0 and 0.08 m s<sup>-1</sup>. Similarly,  $\langle v^a - v_G^a \rangle$  and  $\langle v^{mw} - v_G^{mw} \rangle$  are between 0 and 0.09 m s<sup>-1</sup>, indicating that the dominant mean dynamical balance in the model-only solution is preserved in the assimilation experiments. The magnitudes of  $\langle v^p - v_G^p \rangle$  are typically between 0 and 0.13 m s<sup>-1</sup>, indicating that this nondynamical assimilation typically generated much stronger ageostrophic currents than the model. Sections of  $\sigma_{v^p-v_G^p}$  show that  $v^p$  is also strongly ageostrophic over a much greater region of the shelf compared to  $v^a$  and  $v^m$ . In experiment 2 without the TDAP,  $\sigma_{v^a-v_G^a}$  is of the same magnitude as  $\sigma_{v^p-v_G^p}$ . This indicates that the time-distribution of the correction in the TDAP is necessary to allow the model to effect geostrophic adjustment as the assimilation corrections are gradually introduced into the model. An alternative approach for correcting  $\sigma_\theta$  fields could be to apply a balance constraint, where the corrections to  $\sigma_\theta$  are derived directly from the corrections to  $v$ , subject to the thermal wind relation for example. This approach has not been explored in this study because  $u$  is not necessarily in geostrophic balance and the variable topography makes the identification of an approximate local alongshore direction difficult.

## 7. Summary

[73] A DAS of the subinertial, wind-driven continental shelf circulation off the Oregon coast is described. The DAS assimilates low-pass filtered surface velocity measurements, obtained from land-based HF radars at intervals of approximately 4 hours. The corrections to the model fields are imposed through a TDAP that allows the model dynamics to continuously adjust the analyzed fields so as to preserve appropriate dynamical balances. The DAS utilizes inhomogeneous and anisotropic estimates of the forecast error covariances to distribute the corrections throughout the model domain. In order to demonstrate the capabilities of the DAS, a series of hindcast experiments for a 40-day period during the summer of 1998 is presented. The analyzed fields are partially verified against direct subsurface velocity measurements at one location. Due to a limitation on the number of additional independent observations, the analyzed state could not be validated over an extended spatial domain. However, several features that are generated in the assimilation experiments are qualitatively consistent with recent observations. Furthermore, the validity of the prior error estimates is supported through a series of objective statistical tests. Thus we suggest that the assimilative coupling between the statistically based analysis equations and the dynamically based model should enable an improved estimate of the three-dimensional fields over a region that extends beyond the CODAR array.

[74] The relative magnitude of the forecast and observation error covariances are varied to find the most appropriate

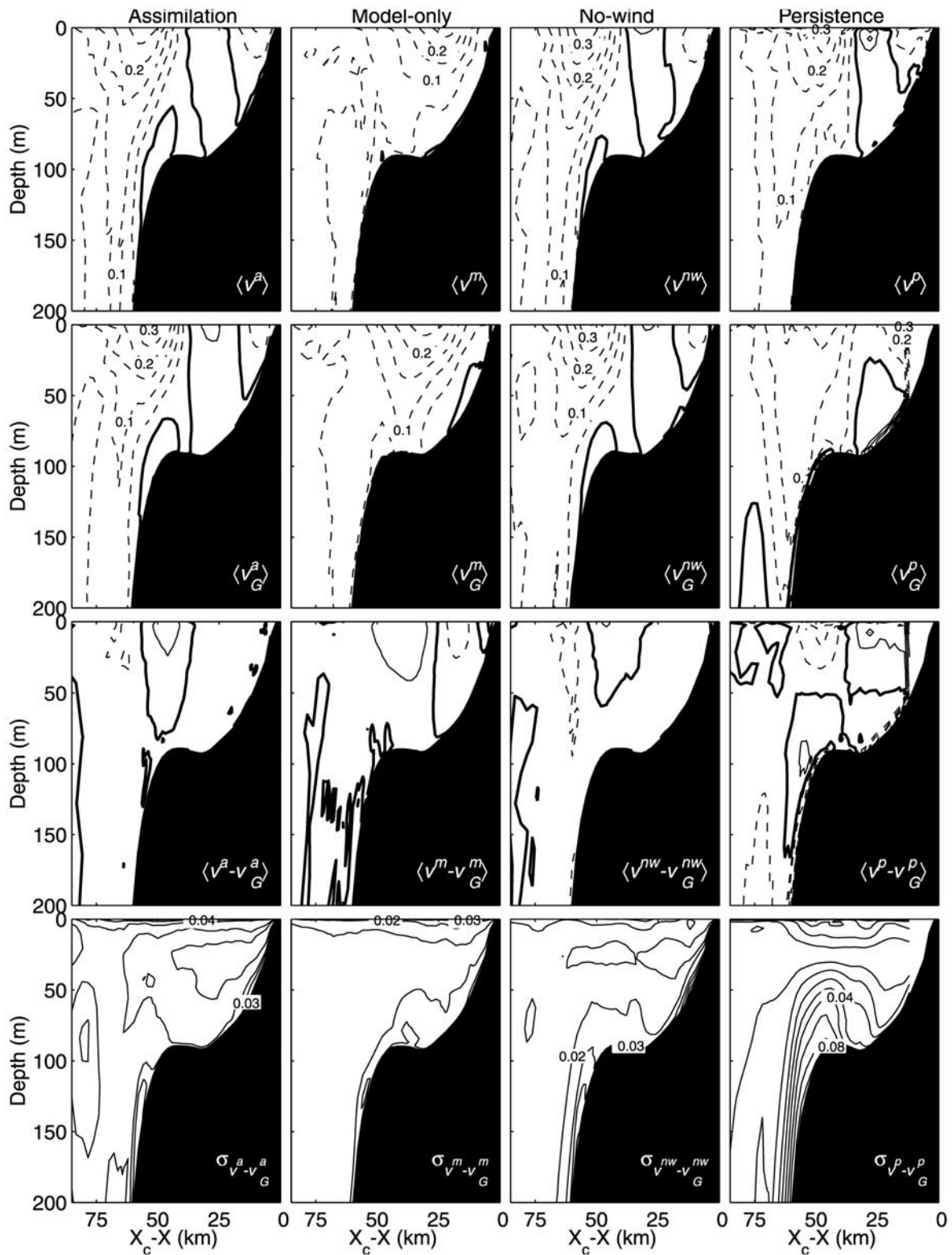


**Figure 19.** Fields of (top to bottom)  $\langle v \rangle$ ,  $\langle v_G \rangle$ ,  $\langle v - v_G \rangle$ , and from (left to right) the assimilation, model-only, no-wind assimilation, and persistence experiments over Heceta Bank (44.25°N) (top three rows,  $\Delta v = 0.05 \text{ m s}^{-1}$ ; dashed line, southward; thick line, zero; bottom row,  $\Delta v = 0.01 \text{ m s}^{-1}$ ).

estimate of the gain in a series of assimilation experiments. As a result, an assessment of the observing system is made, indicating that the DAS is most effective when the analyzed fields are composed of 80% model and 20% observations. This assessment indicates that the model is suitable for use as a dynamical interpolator, constraining the analyzed fields to the dominant physics of the region. It is shown that by introducing the corrections gradually over time, the magnitude of the ageostrophic currents in the assimilation experiment are of the same order as those in the model-only experiment. Conversely, the magnitude of the ageostrophic currents in the persistence experiment are much greater than those in the model-only experiment. We therefore conclude that the gradual imposition of the corrections through the TDAP adequately preserves the expected dominant dynamical balances of the model.

[75] Through an analysis of the  $V$ -equation, and the depth-average of the  $\theta$ -equation, efforts are made to identify the dynamical significance of the correction terms. On the basis of the correlations between the terms in the  $V$ -equation, we hypothesize that one effect of the assimilation is to compensate for unrepresented components of the applied wind stress and wind stress curl. We verify that the lack of spatial variability in the wind field is indeed one source of model error by performing model-only experiments with spatially variable wind, where the spatial structure of the wind is derived from the correction term and observed wind at Newport. This type of analysis might assist the coastal ocean modeling community by identifying the weaknesses of existing models or of specific model configurations, and possibly by identifying which attributes of a model are essential for any given region (e.g., river outflow, surface heating, spatially varying winds, etc.). It is clear that with further development and refinement, simple sequential data assimilation techniques will prove to be very useful from both an operational and scientific perspective. Data assimilation systems, such as the one described here, provide improved physical fields that could be coupled with sediment transport and biogeochemical/ecosystem models.

### Appendix A: Implementation in the POM

[76] The POM uses a mode splitting technique, solving for the depth-averaged barotropic velocity  $\mathbf{V}$  and elevation  $\eta$  more frequently than the baroclinic velocity  $\mathbf{v}$ , the density, and the other baroclinic variables. Before each baroclinic time step,  $\mathbf{v}$  is adjusted by the model so that  $\int_{-1}^0 \mathbf{v} d\sigma = \mathbf{V}$ . It is therefore important that both the barotropic and baroclinic velocities are adjusted by the assimilation procedure in a consistent fashion. This is achieved by calculating the correction term for  $\mathbf{v}$  only, and applying its depth-average to  $\mathbf{V}$ :

$$\mathbf{v}^a = \mathbf{v}^f + \Delta \mathbf{v} \quad (\text{A1})$$

$$\mathbf{V}^a = \mathbf{V}^f + \int_{-1}^0 \Delta \mathbf{v} d\sigma. \quad (\text{A2})$$

The adjustment to  $\eta$  is not applied directly, but rather is accomplished through the tendency term in the barotropic conservation equation:

$$\frac{\partial \eta}{\partial t} + \nabla \cdot (D\mathbf{V}^a) = 0, \quad (\text{A3})$$

where  $\nabla = \mathbf{i}\partial/\partial x + \mathbf{j}\partial/\partial y$  and  $D = h + \eta$ , where  $h$  is the water depth. This approach ensures that both the barotropic and baroclinic conservation equations are satisfied.

### Appendix B: Assessment of Error Estimates

[77] The validity of the estimated forecast error covariances  $\mathbf{P}^f$  is assessed by comparing the magnitude of the elements of the true forecast error  $\epsilon^f$ , determined by subtracting the model forecast  $\mathbf{w}^f$  from the true state of the ocean  $\mathbf{w}^t$ , with the expected standard deviation of the forecast error, denoted by  $\sigma_{\epsilon^f}$ . In reality,  $\mathbf{w}^t$  is never known. Here velocity data from a moored ADP over the mid-shelf off Newport that are not used in the assimilation experiments are considered to be the best available estimate of the truth. This assumption is based on the expectation that  $\epsilon_{ADP}^o \ll \epsilon^f \mathbf{G}^T$ , where  $\mathbf{G}$  is a matrix that interpolates from the model space to the observation space of the ADP measurements. Consequently, we estimate the true forecast error to be

$$\epsilon^f \approx \mathbf{w}_{ADP}^t - \mathbf{G}\mathbf{w}^f. \quad (\text{B1})$$

If the estimate of  $\mathbf{P}^f$  is correct, then  $\epsilon_k^f$  should be less than  $\sigma_{\epsilon_k^f}$  approximately 68% of the time, where

$$\sigma_{\epsilon_k^f} = \left[ (\mathbf{G}\mathbf{P}^f\mathbf{G}^T)_{kk} \right]^{0.5}. \quad (\text{B2})$$

[78] The analysis error covariance matrix  $\mathbf{P}^a$  is defined by

$$\begin{aligned} \mathbf{P}^a &= (\mathbf{I} - \mathbf{K}\mathbf{H})\mathbf{P}^f \\ &\equiv \mathbf{P}^f - \mathbf{P}^f\mathbf{H}^T\mathbf{M}^{-1}(\mathbf{P}^f\mathbf{H}^T)^T, \end{aligned} \quad (\text{B3})$$

and it provides a means by which the validity of the error estimates and the analyzed circulation can be tested. In an analogous fashion to the above-mentioned test of  $\mathbf{P}^f$ , the analysis error can be estimated,

$$\epsilon^a \approx \mathbf{w}_{ADP}^t - \mathbf{G}\mathbf{w}^a, \quad (\text{B4})$$

and  $\epsilon_k^a$  compared to the expected standard deviation of the analysis errors

$$\sigma_{\epsilon_k^a} = \left[ (\mathbf{G}\mathbf{P}^a\mathbf{G}^T)_{kk} \right]^{0.5}. \quad (\text{B5})$$

Again,  $\epsilon_k^a$  should be less than  $\sigma_{\epsilon_k^a}$  approximately 68% of the time.

[79] A comparison between the true and estimated forecast and analysis errors at the ADP site is presented in Figure B1 for experiment 14, showing the percent of time that  $\epsilon_k^{f,a}$  are less than  $\sigma_{\epsilon_k^{f,a}}$ . If the prior and posterior error estimates are correct, then each point in Figure B1 would be 68%. The standard deviations of the errors are underestimated if the percent of time that  $\epsilon_k^{f,a} < \sigma_{\epsilon_k^{f,a}}$  is less than 68%. This analysis indicates that the forecast error estimates of the alongshore velocities  $\epsilon^f v$  at the ADP location are suitable in the upper half of the water column. The error estimates of the analyzed alongshore velocity  $\epsilon^a v$ , and the forecast and analyzed across-shore velocities  $\epsilon^f u$  and  $\epsilon^a u$ , respectively, are underestimated over the entire water column. Although

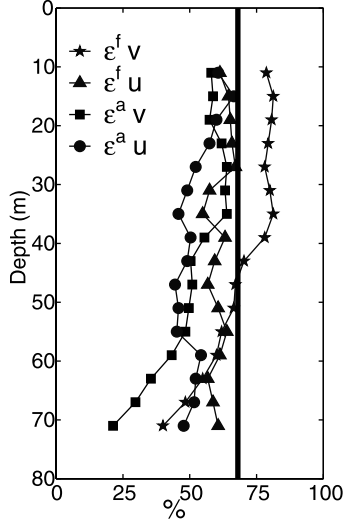


**Figure B1.** The percent of time that  $\epsilon^f$  and  $\epsilon^a$  in the assimilation experiment 14 ( $\beta = 0.4$ , six modes) are less than the expected standard deviations  $\sigma_{\epsilon^f}$  and  $\sigma_{\epsilon^a}$ , respectively, at the ADP location. The 68% level is denoted by the thick vertical line.

this analysis demonstrates that the magnitudes of most of the errors are underestimated at the ADP site, they are typically within the expected ranges for about 50% of the time, instead of the expected 68% of the time. These results indicate that although the magnitude of the error estimates are not exactly correct, they are reasonably close.

### Appendix C: Innovation Statistics

[80] One practical way to assess the optimality of the DAS and the validity of the estimated forecast and observation error covariances is to consider the statistics of the innovations. Recall that the innovation vector  $\delta\mathbf{w} = \mathbf{w}^o - \mathbf{H}\mathbf{w}^f$  is the difference between the observations and the forecasts at each observation location.

#### C1. Optimality

[81] The first measure of the optimality of the assimilation is obtained by considering the whiteness of the innovation sequences. Since white noise contains no systematic information, if the innovation sequence is white in time, then all of the information in the data has been extracted [e.g., Chan *et al.*, 1996]. The whiteness of the innovation sequences can be estimated by considering the autocorrelation function. The lag time of the first zero crossing of the autocorrelation function provides an estimate of the decorrelation timescale of a given sequence. Perfectly white noise has a decorrelation timescale  $T_D$  of zero. As  $T_D$  increases, so does the color of the sequence indicating that information is not efficiently extracted from the data. Since the model variables are expected to fluctuate on timescales that are comparable to the wind, which has a decorrelation timescale of  $T_D(\tau^{Sy}) \approx 2.8$  days, then an acceptable upper timescale for  $T_D(\delta\mathbf{w})$  should be 2.8 days. The decorrelation timescale of the model innovation  $\delta\mathbf{w}^m = \mathbf{w}^o - \mathbf{H}\mathbf{w}^m$ , where

$\mathbf{w}^m$  is the model solution with no assimilation, is 2.4 days, which provides a refined acceptable upper timescale for  $T_D(\delta\mathbf{w})$ . Due to the time averaging employed in the TDAP, we should not expect  $T_D(\delta\mathbf{w})$  to be less than an inertial period  $T_I \approx 0.7$  days. Thus, if  $T_I < T_D(\delta\mathbf{w}) < T_D(\delta\mathbf{w}^m)$ , we can conclude that information is being extracted from the data at an acceptable level for the suboptimal scheme being employed here.

#### C2. Chi-Squared Test

[82] In order to determine whether the distributions of the actual innovation covariances are consistent with the estimated innovation covariance matrix  $\mathbf{M}$ , we consider the variable

$$\mathbf{X}^2 = \delta\mathbf{w}^T \mathbf{M}^{-1} \delta\mathbf{w}, \quad (\text{C1})$$

which should have a  $\chi^2$  distribution with  $p$  degrees of freedom, where  $p$  is the number of observations used in each assimilation. This assumes that  $\delta\mathbf{w}$  is normally distributed with zero mean. The mean values of  $\delta\mathbf{w}$  and  $\delta\hat{\mathbf{w}}$  are  $-0.03 \pm 0.027 \text{ m s}^{-1}$  and  $-0.0016 \pm 0.034 \text{ m s}^{-1}$ , respectively, indicating that the above-mentioned assumption is valid for this application. Therefore  $\langle \mathbf{X}^2 \rangle$  should equal  $p$ , where for example  $p = 18$  for experiments 5–7 with no EVD. Furthermore, the standard deviation  $\sigma_{\mathbf{X}^2}$  should be approximately  $\sqrt{2p} = 6$  for a  $\chi^2$  distribution with 18 degrees of freedom. For the EVD approach, the data is first projected onto its orthogonal modes with only  $m$  of the modes used in each assimilation. In those cases an equivalent statistic to  $\mathbf{X}^2$  is  $\hat{\mathbf{X}}^2$ ,

$$\hat{\mathbf{X}}^2 = \delta\hat{\mathbf{w}}^T \hat{\Lambda}^{-1} \delta\hat{\mathbf{w}}, \quad (\text{C2})$$

which should have a  $\chi^2$  distribution with  $m$  degrees of freedom. Therefore  $\langle \hat{\mathbf{X}}^2 \rangle$  should equal  $m$  for the assimilation experiments that utilize the EVD approach, and  $\sigma_{\hat{\mathbf{X}}^2}$  should be approximately  $\sqrt{2m}$ .

#### C3. Results

[83] In order to summarize these diagnostic statistics for all of the experiments in a single figure,  $\langle \hat{\mathbf{X}}^2 \rangle$  and  $\sigma_{\hat{\mathbf{X}}^2}$  are normalized:

$$\| \langle \hat{\mathbf{X}}^2 \rangle \| = \frac{\hat{\mathbf{X}}^2}{m} \quad (\text{C3})$$

$$\| \sigma_{\hat{\mathbf{X}}^2} \| = \frac{\sigma_{\hat{\mathbf{X}}^2}}{\sqrt{2m}}, \quad (\text{C4})$$

where  $m$  is the number of modes used in the EVD of  $\mathbf{M}$  in equation (6).

[84] A summary of the innovation statistics outlined above are presented in Figure C1 for experiments 2–23. For all of the assimilation experiments,  $T_D(\delta\mathbf{w})$  is approximately 1.5 days (Figure C1), which falls within the acceptable range as outlined above. This indicates that although the assimilation scheme is not optimal it is capable of extracting information from the innovations within the acceptable timescales.

[85] If the  $\chi^2$  test is satisfied then one cannot reject the hypothesis that the prior error estimates are valid. The values

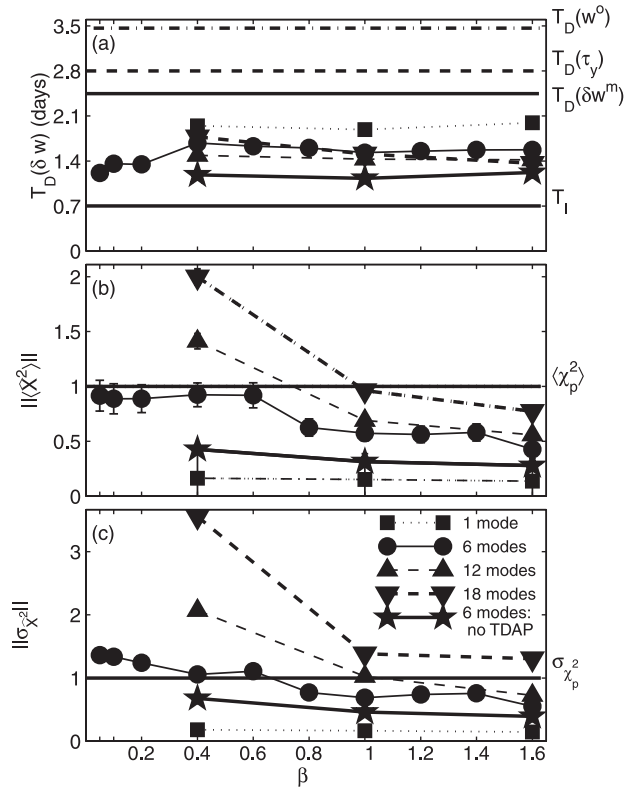


**Figure C1.** (a) Decorrelation timescale of  $\delta w$ ; (b)  $\|\langle \hat{X}^2 \rangle\|$  and the theoretical  $\langle \chi_p^2 \rangle$  (thick line); and (c)  $\|\sigma_{\hat{X}^2}\|$  and the theoretical  $\sigma_{\chi_p^2}$  (thick line) for assimilation experiments 2–23 described in Table 1 with various number of modes in equation (6) and for different values for  $\beta$  in equation (12).

of  $\|\langle \hat{X}^2 \rangle\|$ , defined in equation (C3) indicate that the above-mentioned criterion is satisfied for  $\beta \leq 0.6$  when six modes are used, for  $0.8 \leq \beta \leq 1.0$  when 12 modes are used, and for  $\beta = 1.6$  when 18 modes are used. Additionally, the values of  $\|\sigma_{\hat{X}^2}\|$ , indicate that the hypothesis about the prior error statistics cannot be rejected for  $\beta = 0.4$  or  $0.6$  when six modes are used and for  $\beta = 1.0$  when 12 modes are used. Therefore,

consideration of both the mean and standard deviations of  $\hat{X}^2$  indicates that the prior error estimates for the experiments using six modes with  $\beta = 0.4$  or  $0.6$  cannot be rejected.

[86] Examples of the empirical probability density function (PDF) of  $\hat{X}^2$  (scaled histogram) are presented in Figure C2 for the experiments using six modes with  $\beta = 0.4$  and  $1.0$ . These two experiments provide examples of distributions of  $\hat{X}^2$  when the  $\chi^2$  test is satisfied ( $\beta = 0.4$ ) and is not satisfied ( $\beta = 1.0$ ).

[87] The statistical tests described above assess the validity of the estimated forecast and observation error statistics  $\mathbf{P}^f$  and  $\mathbf{R}$ , respectively. When considered with the assessments of the analyzed subsurface velocities at the ADP location, in section 5, we conclude that the best analysis is produced when six modes are used in the EVD of  $\mathbf{M}$  and  $\beta \geq 0.4$ . Furthermore, the tests indicate that the hypothesis about the prior error statistics cannot be rejected for the experiments when six modes are used and  $\beta = 0.4$  or  $0.6$ .

#### Appendix D: Persistence Experiments

[88] A persistence experiment [e.g., *Murphy, 1992*] involves a statistical model that utilizes observations and estimated error covariance statistics without the benefit of a dynamical model and is implemented given an initial condition  $\mathbf{w}_0$  and a time series of observations  $\mathbf{w}_{1..N}^o$ . By utilizing the estimated forecast and observation error covariances that are used to formulate the gain matrix  $\mathbf{K}$  defined in equation (2), a persistence analysis  $\mathbf{w}_{1..N}^p$  can be obtained sequentially by solving a form of equation (1),

$$\mathbf{w}_1^p = \mathbf{w}_0 + \mathbf{K}(\mathbf{w}_1^o - \mathbf{H}\mathbf{w}_0) \quad (\text{D1})$$

$$\mathbf{w}_2^p = \mathbf{w}_1^p + \mathbf{K}(\mathbf{w}_2^o - \mathbf{H}\mathbf{w}_1^p) \quad (\text{D2})$$

⋮

$$\mathbf{w}_N^p = \mathbf{w}_{N-1}^p + \mathbf{K}(\mathbf{w}_N^o - \mathbf{H}\mathbf{w}_{N-1}^p). \quad (\text{D3})$$

Such experiments are commonly used in numerical weather forecasting as a kind of zero-skill base from which to evaluate

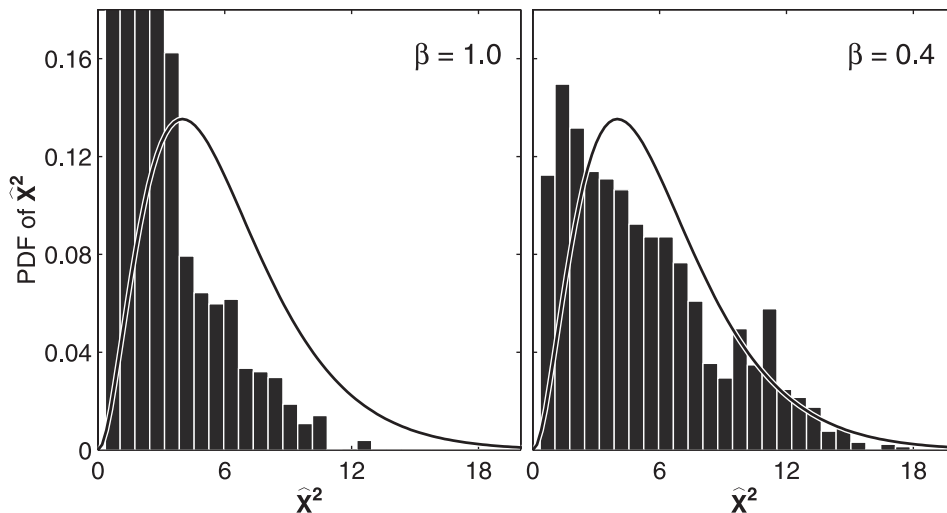


**Figure C2.** Distributions of  $\hat{X}^2$  (from equation (C2)) for  $\beta = 1.0$  and  $0.4$  with the expected  $\chi_6^2$  probability density functions overlaid.

more sophisticated forecast systems [e.g., Fraedrich and Leslie, 1988]. In our applications, the initial conditions are the model fields at the end of the 10-day spin-up period.

[89] **Acknowledgments.** This research was supported by the National Oceanographic Partnership Program (NOPP) through ONR grant N00014-98-1-0787. Support was also provided by the ONR Ocean Modeling and Prediction Program through grant N00014-98-1-0043 and by an ONR DURIP grant N00014-99-1-0773. The authors thank Alexandre Kurapov and Jay Austin for helpful discussions during the course of this research.

## References

- Allen, J. S., Models of wind-driven currents on the continental shelf, *Ann. Rev. Fluid Mech.*, **12**, 389–433, 1980.
- Allen, J. S., P. A. Newberger, and J. Federiuk, Upwelling circulation on the Oregon Continental Shelf, I, Response to idealized forcing, *J. Phys. Oceanogr.*, **25**, 1843–1866, 1995.
- Baker, W. E., S. Bloom, J. Woollen, M. Nestler, E. Brin, T. Schlatter, and T. Branstator, Experiments with a three-dimensional statistical objective analysis scheme using FGGE data, *Mon. Weather Rev.*, **115**, 272–296, 1987.
- Barrier, B., P. Marchesiello, A. Pimenta de Miranda, M. Coulibaly, and J. M. Molines, A sigma-coordinate primitive equation model for studying the circulation in the South Atlantic, I, Model configuration with error estimates, *Deep Sea Res. Part I*, **45**, 543–572, 1998.
- Bartello, P., and H. L. Mitchell, A continuous three-dimensional model of short-range forecast error covariances, *Tellus, Ser. A*, **44**, 217–235, 1992.
- Barth, J. A., R. O'Malley, A. Y. Erofeev, J. Fleischbein, S. D. Pierce, and P. M. Kosro, SeaSoar CTD observations from the Central Oregon Shelf, W9907C, 13–31 July, 1999, *Rep. 184 Ref. 2001-5*, Coll. of Oceanic and Atmos. Sci., Oreg. State Univ., Corvallis, 2001.
- Bennett, A. F., Array design by inverse methods, *Prog. Oceanogr.*, **15**, 129–151, 1985.
- Bennett, A. F., *Inverse Methods in Physical Oceanography*, 156 pp., Cambridge Univ. Press, New York, 1992.
- Bloom, S. C., L. L. Takacs, A. M. Da Silva, and D. Ledvina, Data assimilation using incremental analysis updates, *Mon. Weather Rev.*, **124**, 1256–1271, 1996.
- Blumberg, A. F., and L. H. Kantha, Open boundary conditions for circulation models, *J. Hydrol. Eng.*, **111**, 237–255, 1985.
- Blumberg, A. F., and G. L. Mellor, A description of a three-dimensional coastal ocean circulation model, in *Three-Dimensional Coastal Ocean Models*, *Coastal Estuarine Stud.*, vol. 4, edited by N. Heaps, pp. 1–16, AGU, Washington, D. C., 1987.
- Brink, K. H., and J. S. Allen, On the effect of bottom friction on barotropic motion over the continental shelf, *J. Phys. Oceanogr.*, **8**, 919–922, 1978.
- Brunk, H. D., *An Introduction to Mathematical Statistics*, 221 pp., Blaisdell, New York, 1965.
- Chan, N. H., J. B. Kadane, R. N. Miller, and W. Palma, Estimation of tropical sea level anomaly by an improved Kalman filter, *J. Phys. Oceanogr.*, **26**, 1286–1303, 1996.
- Chapman, D. C., Numerical treatment of cross-shelf open boundaries in a barotropic coastal ocean model, *J. Phys. Oceanogr.*, **15**, 1060–1075, 1985.
- Chen, C. S., and D. P. Wang, Data assimilation model study of the Santa Barbara Channel circulation, *J. Geophys. Res.*, **104**, 15,727–15,741, 1999.
- Cohn, S. E., and D. F. Parrish, The behaviour of forecast error covariances for a Kalman filter in two dimensions, *Mon. Weather Rev.*, **119**, 1757–1785, 1991.
- Cohn, S. E., A. da Silva, J. Guo, M. Sienkiewicz, and D. Lamich, Assessing the effects of data selection with the DAO Physical-space Statistical Analysis System, *Mon. Weather Rev.*, **126**, 2913–2926, 1998.
- Daley, R., *Atmospheric Data Analysis*, 45 pp., Cambridge Univ. Press, New York, 1993.
- Enriquez, A. G., and C. A. Friehe, Effects of wind stress and wind stress curl variability on coastal upwelling, *J. Phys. Oceanogr.*, **25**, 1651–1671, 1995.
- Ezer, T., and G. L. Mellor, Data assimilation experiments in the Gulf Stream region: How useful are satellite-derived surface data for nowcasting the subsurface fields?, *J. Atmos. Oceanic Technol.*, **14**, 1379–1391, 1997.
- Federiuk, J., and J. S. Allen, Upwelling circulation on the Oregon Continental Shelf, II, Simulations and comparisons with observations, *J. Phys. Oceanogr.*, **25**, 1867–1889, 1995.
- Fraedrich, K., and L. M. Leslie, Real-time short-term forecasting of precipitation at an Australian tropical station, *Weather Forecasting*, **3**, 104–114, 1988.
- Ghil, M., and P. Malanotte-Rizzoli, Data assimilation in meteorology and oceanography, *Adv. Geophys.*, **33**, 141–266, 1991.
- Hurlburt, H. E., Dynamic transfer of simulated altimeter data into subsurface information by a numerical ocean model, *J. Geophys. Res.*, **91**, 2372–2400, 1986.
- Kundu, P. K., Ekman veering observed near the ocean bottom, *J. Phys. Oceanogr.*, **6**, 238–242, 1976.
- Kurapov, A. L., G. D. Egbert, R. N. Miller, and J. S. Allen, Data assimilation in a baroclinic coastal ocean model: Generalized inverse, *Mon. Weather Rev.*, **130**, 1009–1025, 2002.
- Leise, J. A., The analysis and digital signal processing of NOAA's surface current mapping system, *IEEE J. Oceanic Eng.*, **OE-9**, 106–113, 1984.
- Lentz, S. J., and C. D. Winant, Subinertial currents on the Southern California Shelf, *J. Phys. Oceanogr.*, **16**, 1737–1750, 1986.
- Lewis, J. K., I. Shulman, and A. F. Blumberg, Assimilation of Doppler radar current data into numerical ocean models, *Cont. Shelf Res.*, **18**, 541–559, 1998.
- Lipa, B. J., and D. E. Barrick, Least-squares methods for the extraction of surface currents from CODAR cross-loop data: Application at ARSLOE, *IEEE J. Oceanic Eng.*, **OE-8**, 226–253, 1983.
- Lynch, P., and X. Y. Huang, Initialization of the HIRLAM model using a digital filter, *Mon. Weather Rev.*, **120**, 1019–1034, 1992.
- Mellor, G. L., and T. Yamada, Development of a turbulence closure model for geophysical fluid problems, *Rev. Geophys.*, **20**, 851–875, 1982.
- Mellor, G. L., T. Ezer, and L.-Y. Oey, The pressure gradient conundrum of sigma coordinate ocean models, *J. Atmos. Oceanic Technol.*, **11**, 1126–1134, 1994.
- Miller, R. N., Toward the application of the Kalman filter to regional open ocean modeling, *J. Phys. Oceanogr.*, **16**, 72–86, 1986.
- Murphy, A. H., Climatology, persistence, and their linear combination as standards of reference in skill scores, *Weather Forecasting*, **7**, 692–698, 1992.
- Oke, P. R., J. S. Allen, R. N. Miller, G. D. Egbert, J. A. Austin, J. A. Barth, T. J. Boyd, P. M. Kosro, and M. D. Levine, A modeling study of the three-dimensional continental shelf circulation off Oregon, I, Model-data comparisons, *J. Phys. Oceanogr.*, **32**, 1360–1382, 2002a.
- Oke, P. R., J. S. Allen, R. N. Miller, and G. D. Egbert, A modeling study of the three-dimensional continental shelf circulation off Oregon, II, Dynamical analysis, *J. Phys. Oceanogr.*, **32**, 1383–1403, 2002b.
- Paduan, J. D., and L. K. Rosenfield, Remotely sensed surface currents in Monterey Bay from shore-based HF radar (Coastal Ocean Dynamics Application Radar), *J. Geophys. Res.*, **101**, 20,669–20,686, 1996.
- Parker, R. L., *Geophysical Inverse Theory*, 144 pp., Princeton Univ. Press, Princeton, N. J., 1994.
- Parrish, D. F., and J. C. Derber, The National Meteorological Center's spectral-interpolation analysis system, *Mon. Weather Rev.*, **120**, 1747–1763, 1992.
- Rienecker, M. M., and D. Adamec, Assimilation of altimeter data into a quasi-geostrophic ocean model using optimal interpolation and EOF's, *J. Mar. Syst.*, **6**, 125–143, 1995.
- Rienecker, M. M., and R. N. Miller, Ocean data assimilation using optimal interpolation with a quasi-geostrophic model, *J. Geophys. Res.*, **96**, 15,093–15,103, 1991.
- Rutherford, I. D., Data assimilation by statistical interpolation of forecast error fields, *J. Atmos. Sci.*, **29**, 809–815, 1972.
- Samelson, R. M., P. Barbour, J. Barth, S. Bielli, T. Boyd, D. Chelton, P. Kosro, M. Levine, E. Skyllingstad, and J. Wilczak, Wind stress forcing of the Oregon coastal ocean during the 1999 upwelling season, *J. Geophys. Res.*, **107**, 10.1029/2001JC000900, 2002.
- Scott, R. K., J. S. Allen, G. D. Egbert, and R. N. Miller, Assimilation of surface current measurements in a coastal ocean model, *J. Phys. Oceanogr.*, **30**, 2359–2378, 2000.
- Smagorinsky, J., General circulation experiments with primitive equations, I, The basic experiment, *Mon. Weather Rev.*, **91**, 99–164, 1963.
- Smedstad, O. M., and D. N. Fox, Assimilation of altimeter data into a two-layer primitive equation model of the Gulf Stream, *J. Phys. Oceanogr.*, **24**, 305–325, 1994.
- Smith, S. W., *The Scientist and Engineer's Guide to Digital Signal Processing*, 277 pp., Calif. Tech. Publ., San Diego, Calif., 1997.
- Stauffer, D. R., and N. L. Seaman, Use of four-dimensional data assimilation in a limited-area mesoscale model, I, Experiments with synoptic-scale data, *Mon. Weather Rev.*, **118**, 1250–1277, 1990.

J. S. Allen, G. D. Egbert, P. M. Kosro, and R. N. Miller, College of Oceanic and Atmospheric Sciences, Oregon State University, 104 Ocean Administration Building, Corvallis, OR 97331-5503, USA. (jallen@coas.oregonstate.edu; egbert@coas.oregonstate.edu; kosro@coas.oregonstate.edu; miller@coas.oregonstate.edu)

P. R. Oke, School of Mathematics, University of New South Wales, Sydney, 2052, Australia. (petero@maths.unsw.edu.au)